Toluene and Styrene Photo-Oxidation Quantum Efficiency: Comparison between Doped and Composite Tungsten-containing Anatase-based Catalysts

Uriel Caudillo-Flores,[1] Mario J. Muñoz-Batista,[1,2] Ana B. Hungría,[3] Miguel López Haro,[3] Marcos Fernández-García, [1,*] Anna Kubacka,[1,*]

1 Instituto de Catálisis y Petroleoquímica, CSIC, C/Marie Curie 2, 28049-Madrid, Spain

2. Departamento de Quımica Organica, Universidad de Cordoba, Edificio Marie-Curie (C-3), Ctra Nnal IV-A, Km 396, Cordoba, Spain.

3. Departamento de Ciencia de Materiales, Ingeniería Metalúrgica y Química Inorgánica, Facultad de Ciencias, Universidad de Cádiz, 11510 Puerto Real, Cádiz, Spain

Abstract

In this work we analyze two series of samples containing tungsten and titania as cations with a W/Ti atomic ratio from 0 to 0.5. The samples are prepared by a single-pot procedure, rendering in all cases high surface area powders having a dominant anatase crystalline phase. The materials were characterized by a combination of X-ray diffraction and photoelectron spectroscopies, UV-visible and Raman spectroscopies and morphological measurements. Particular effort was carried out in analyzing the way tungsten and titania interact in the materials through a microscopy analysis combining dark field Scanning transmission electron microscopy (HAADF-STEM) an X-ray energy dispersive spectrometry (XEDS). Overall the results are able to spot out the samples that show a truly doped character with tungsten exclusively located at (surface and bulk) lattice positions of the anatase structure, from composite catalysts where nanosized tungsten entities are supported over the dominant anatase phase. Activity of the materials in toluene and styrene photo-transformation reactions was measured through the reaction rate and the quantum efficiency observables. The study shows that quantitative comparison requires the stringent calculation of the quantum efficiency and that both the reaction rate and the apparent quantum efficiency can lead to misleading results in terms of the most active sample(s) as well as the (positive/negative) magnitude with respect to the bare titania reference. The quantum efficiency shows that doped samples can always improve titania reference sample(s) while this is not the case for composite samples.

1. Introduction

Pollution appears as a prime factor in environmental as well as human heald related problems of industrialized societies. To mitigate the adverse effects of pollution, scientific attention has been focused on controlling (pollution) sources as well creating depollution technologies. Among the latter, heterogeneous photocatalysis is a promising technology that uses semiconductors and light to control and reduce harmful entities in liquid and gas effluents or streams. Its main field of application corresponds to the degradation and/or transformation of organic and inorganic pollutants as well as biological microorganisms (1,2,3,4). Titania and particularly the anatase polymorph appear as the central semiconductor system in photocatalysis. The universal application of titania for photo-degradation or photo-transformation of organic and inorganic molecules is a well known fact. Nevertheless, the activity level typically obtained in photo-catalysis by titania samples is limited (1-4). Doping and surface sensitization of titania-based catalysts are two of the ways broadly applied in order to obtain highly active photo-catalysts. They optimize or improve the activity of the bare titania reference materials by addition of an alien species, being in the majority of cases titania the main (by weight) component of the catalyst formulation (1-4,5,6). Very few metal-containing species can work efficiently in both types of technologies. Tungsten corresponds to one of them. Tungsten doping of titania has been claimed to be particularly effective in the degradation (total-oxidation) of hydrocarbons (7,8,9), pesticides (10), or dyes (11,12,13,14,15,16), and (mostly) partial oxidation of chlorophenols (11,13,17) styrene (18,19,20) and pharmaceuticals (21). Similarly tungsten surface species present at the surface of titania-based materials were shown effective in total-oxidation of hydrocarbons (22,23), alcohols (24), dyes (25,26) as well as partial oxidation reactions of organics, like styrene (27), butyl-acetate (28), 2-propanol (29,30), chlorophenols (31), and oxalic acid (32).

However when analyzing the performance of tungsten doped vs. tungsten surface sensitized (titania-based) materials, we do not have a clear vision of the relative performance of (doped vs. sensitized) samples having equal chemical compositions. Apart from the fact that both technologies can improve the operation of bare titania materials, it is difficult to obtain an unquestionable answer to the real promotion effect. Several problems contribute to this issue. First, materials are often not obtained using similar preparation procedures and, probably more important, they are not subject to

similar calcination procedures which can thus render dissimilar morphological properties related to surface area, porosity, primary particle size and others. Moreover, the alien species can trigger the generation of different titania phases after calcination when predominantly presented at the surface or the bulk (1,3). Second, the frontier between doping and surface sensitization is not obvious. Some catalysts presenting a single anatase or rutile phase can show surface enrichment in the alien species and the nuclearity of such entities is difficult to be assessed without doubt. This last fact precludes to define samples containing XRD (also Raman) silent (surface) phase(s) as surface termination of doped materials or, contrarily, of incipient composite systems. This can lead to an imprecise or erroneous analysis of the catalytic role of the surface (sensitizing) phases. Finally, the absence of reports presenting the true quantum efficiency of the reaction further precludes a clear comparison of the catalytic performance of these two types of materials which can differ significantly in optical properties while having equal atomic composition.

In this contribution we attempt for the first time to avoid all these problems by using a single-pot synthetic procedure rendering high surface area materials in all cases, for doped and surface sensitized anatase-based materials having tungsten as alien species. Using up to date microscopy and spectroscopic techniques, we explore also the surface termination of the materials in order to clarify the presence of diffraction silent surface species and their potential catalytic role. The materials are specifically synthesized for this study although we previously obtained relatively similar doped or sensitized materials but using slightly different preparation procedures and, particularly, different calcination treatments (8,27). By applying a multitechnique study of the materials we analyzed their structural and electronic properties. This would provide a firm ground to interpret catalytic activity in toluene and styrene photo-oxidation reactions. Toluene is chosen as a benchmark for a photo-degradation reaction of an organic pollutant present in urban atmospheres (33) while styrene is chosen as an example of a photo-synthesis reaction to render high added value commodities of industrial interest (34). They are also chemically close molecules, facilitating that the comparison of results would focus on the catalyst(s) performance. To provide a truly quantitative analysis of the comparison we measure the quantum efficiency of the reaction using the rigorous formulation and including the calculation the local surface volumetric rate of photon absorption as well as the number of charge carrier used to produce each reaction product (35). The latter is particularly important for comparing catalysts mostly working as

depollution (total oxidation) photo-materials from those acting as partial oxidation materials aiming to render industrially relevant chemicals. This will come out from the significantly different number of charge carriers involved in the generation of the reaction products of these two types of processes. Using thus this approach, this contribution pretends to present valuable (and up to now absent in the literature according to the authors knowledge) information comparing tungsten doping and surface sensitization of pure anatase-based systems.

2. Materials and methods
2.1. Sample preparation and characterization

Samples were synthesized using a microemulsion method in a single pot for both surface sensitized and doped samples. The microemulsion consisted in an aqueous phase dispersed in *n*-heptane, using Triton X-100 (Aldrich) as surfactant and hexane as cosurfactant (36). Titanium tretraisopropoxide (Aldrich) and ammonium tungsten oxide (Alfa Aesar) were used in all synthesis procedures. Total cation content of the aqueous solution is 0.5 M. Water/(Ti+W) and water/surfactant molar ratios were, respectively, 18 and 110 for all samples.

In the case of surface sensitized samples the aqueous solution of the tungsten precursor was agitated for 30 min. Subsequently, a stoichometric (to obtain the corresponding W(VI) hydroxide) quantity of tetramethylammonium-hydroxide (TMAH) was introduced from the aqueous phase of a similar microemulsion. After 5 min of contact, titanium tetraisopropoxide was introduced into the previously resulting microemulsion drop by drop from a mixture with isopropanol (2:3). In the case of doped samples, we added Titanium tetraisopropoxide (mixed with isopropanol as before) to an inverse emulsion containing an aqueous solution of the tungsten precursors (previously agitated for 30 minutes). In both types of samples, the resulting mixtures were stirred for 24 h, centrifuged, decanted, rinsed with methanol and dried at 300 K for 6 h. Following the microemulsion preparation method, the amorphous powders were calcined under air for 2 h at 723 K. Calcination temperature was selected (in the 673-873 K range) to obtain at least one doped and one composite samples with activity above the anatase reference in both reaction tested. Chemical composition of the solids was measured using total reflection x-ray fluorescence (Bruker - S2 PicoFox TXRF Spectrometer). Samples names are WxTiy (where x and y correspond to the atomic content percentage in cation

basis) for doped samples and zWO_3/TiO_2 (where z is the tungsten oxide moles per 1 mol of titania) for composite samples.

The BET surface areas and average pore volumes and sizes were measured by nitrogen physisorption (Micromeritics ASAP 2010). XRD profiles were obtained using a Seifert D-500 diffractometer using Ni-filtered Cu Kα radiation with a 0.02° step. The particle sizes were estimated using XRD using the Williamson–Hall formalism (37). UV–vis diffuse-reflectance spectroscopy experiments were performed on a Shimadzu UV2100 apparatus using nylon as a reference and the results presented as Kubelka-Munk transform (38). Band gap analysis for the titania (anatase) indirect gap semiconductor was done following standard procedures; e.g. plotting $(hva)^n$ (n= ½ or 2 for indirect or direct semiconductor; hv =excitation energy, a=absorption coefficient) vs. energy and obtaining the corresponding intersection of the linear fit with the baseline (39). Raman spectroscopic analyses of the samples were carried out with a Jobin-Ibon iHR320 spectrometer. Photoluminescence spectra were measured at room temperature on a Fluorescence Spectrophotometer (Perkin Elmer LS50B).

XPS data were recorded on 4×4 mm^2 pellets, 0.5 mm thick, prepared by slightly pressing the powered materials which were outgassed in the prechamber of the instrument at room temperature up to a pressure $<2 \times 10^{-8}$ Torr to remove chemisorbed water from their surfaces. The SPECS spectrometer main chamber, working at a pressure $< 10^{-9}$ Torr, was equipped with a PHOIBOS 150 multichannel hemispherical electron analyzer with a dual X-ray source working with Ag Kα ($hv = 1486.2$ eV) at 120 W, 20 mA using C 1s as energy reference (284.6 eV). Surface chemical compositions were estimated from XP-spectra, by calculating the integral of each peak after subtraction of the "S-shaped" Shirley-type background (40) using the appropriate experimental sensitivity factors and the CASA-XPS (version 2.3.15) software.

Catalysts were also characterized by High Angle Annular Dark Field Scanning Transmission Electron Microscopy (HAADF-STEM) using two different microscopes. A general analysis of the samples was made in a JEOL-2010F microscope with a structural resolution of 0.19 nm in TEM. HAADF-STEM images were recorded using a 0.5 nm electron probe at a camera length of 10 cm. This microscope was equipped with an X-ray Energy Dispersive Spectrometer (X-EDS) from Oxford Instruments, model Xmax SSD, for compositional analysis at the subnanometer scale. The most representative samples were studied in a FEI Titan^3 Themis 60-300 Double Aberration Corrected (AC) microscope operated at 200kV. The aberrations of the condenser lenses

were corrected up to third-order using the Zemlin tableau to obtain a sub-Angstrom electron probe. A condenser aperture of 50 µm yielding an electron probe with a convergence angle of 20 mrad was used.

The compositional maps were performed by X-ray Energy Dispersive Spectroscopy in STEM mode (STEM-XEDS) using the FEI Titan[3] Themis 60–300 microscope which is equipped with the SuperX G2 detector. Very high spatial resolution STEM-XEDS maps were acquired using a high brightness, sub-angstrom diameter, electron probe in combination with a highly stable stage which minimized sample drift. Element maps were acquired with a beam current of 80-120 pA and a dwell time of 100 ms which results in a total acquisition time of approximately 15 minutes. The quantitative analyses were carried out on Ti K and W L lines using calculated K-factors, taking into account the ionization cross-section Shcreiber-Wimm model, which is provided by Velox 2.4.1 software.

2.2. Photo-catalytic experimental and computational details

Gas-phase photo-oxidation of toluene (≥99% Aldrich) was carried in a continuous flow annular photoreactor containing ca. 0.4 mg cm^{-2} of photocatalyst as a thin layer coating on a pyrex tube. The reactor details are fully described in a previous work and a scheme of it is presented in Figure 1 (41). The reacting mixture (100 mL min^{-1}) was prepared by injecting toluene into a wet (ca. 75% relative humidity) 20 vol.% O_2/N_2 flow before entering to the photoreactor, yielding an organic inlet concentration of ca. 700 ppmv. Fluorescent UV (Sylvania F6WBLT-65; 6 W) lamps were used for the photoreaction experiment. Reaction rates and selectivity were evaluated under steady-state conditions, typically achieved after ca. 2 h from the irradiation starting. The concentration of toluene and the reaction products were analyzed using an on-line gas chromatograph (Agilent GC 7890B) equipped with a TCD (for CO_2 measurement) and FID (organics measurement) detectors. Catalytic results are stable for 24 h of continuous flow operation. Carbon balance was better than 95.5 % for all cases here presented.

Catalytic measurements were here presented by calculation of the true quantum efficiency. To this end we first calculated the local superficial rate of photon absorption ($e^{a,s}$) as defined by Equation 1 (41). In this equation F_{A_S} is the fraction of light absorbed by the sample and q_{sup} the radiation flux at each position ($\underline{x} \equiv X_s, Y_s, Z_s$) of the catalytic film (See Figure 1).

$$e^{a,s}(\underline{x}) = q_{sup}(\underline{x})\,F_{A_s}$$

(1)

To obtain the radiation flow on the surface of the samples, we calculate first the impinging radiation flux from the lamps (q_n in Figure 1). Considering the coordinate system presented in Figure 1 and the geometry of the reactor (annular multilamp), the q_n can be determined by Equation 2 (41).

$$q_n\,(X_s, Y_s, Z_s) = \sum_{L=1}^{L=4} \sum_\lambda \int_{\varphi min,L(x,y)}^{\varphi max,L(x,y)} \int_{\theta min(x,y,\varphi)}^{\theta max(x,y,\varphi)} \frac{P_{\lambda,L}}{2\pi\,R_L\,Z_L}\,\sin^2\theta\,\left(\left(\frac{X_s - X_L}{R}\right)\cos\varphi + \right.$$

$$\left. \left(\frac{y_s}{R}\right)\sin\varphi\right)d\varphi d\theta$$

(2)

Where Xs, Ys, Zs and R are the coordinates of the points located on the surface of the catalytic films and the radius of the cylinder supporting the sample (Figure 1). Angle variables (θ, φ) are defined as described in Figure 1. The integration limits can be evaluated using the ray tracing method (41), and are presented in the supporting information section.

Finally, the q_{sup} x/y components (see Figure 1; Equation 3) can be determined using q_n and a radiation balance, which considers the main optical (Transmittance, F_i, and Reflectance, R_i) events occurring in all components of the reactor placed between the emission source and catalyst, i.e. glass and reaction media, as well on the catalytic film.

$$q_{sup}^{x,y} = f\,(\,q_n, F_i, R_i);\,i = catalyst, glass, reaction\,media$$

(3)

A detailed description of the mathematical formulation to provide q_{sup} as a function of q_n (Equation 2) and the transmittance/reflectance optical measurements for each component of our reactor system can be found elsewhere (41,42).

Quantum efficiency values (η_q) were determined using Equation 4 (35). This work presents the determination of the true quantum efficiency according to the IUPAC recommendation by dividing the reaction rate (r: mol m^{-2} s^{-1}) with the averaged superficial rate of photon absorption ($< e^{a,s} >$: Einstein m^{-2} s^{-1}) multiplied by the factor concerning the number of charge species involved for the generation of each reaction product (factor S, dimensionless).

$$\eta_q(\%) = 100 \times \frac{r}{S < e^{a,s} >}$$

(4)

Where the S factor (also called selectivity factor) is calculated as a summation over all chemical reactions consuming the reactive (toluene or styrene) and takes the value:

$$S = \sum_i n_i \, S_i \tag{5}$$

Where S_i is the fractional selectivity to product i, and n_i is the inverse of number of charge carrier species required to per mol of reactive (41). As explained below the S factor takes into account the (different) number of photons used in the generation of the different products of the chemical reaction.

We also presented the apparent quantum efficiency which follows equation 6.

$$\eta_a(\%) = 100 \times \frac{r}{Q} \tag{6}$$

Where all symbols where previously defined except Q, the photon flux (measured here using a radiometer HD2303 Delta Ohm).

3. Results and discussion

3.1. Characterization results

Here we have synthesized two series of samples having tungsten and titanium as cations and prepared them by a relatively similar single-pot microemulsion procedure followed by the same calcination treatment. Chemical analysis was used to measure the cation content of the samples. Specifically, the W/Ti atomic ratio measured is 0.11, 0.23, 0.41 for, respectively, the W10Ti90, W20Ti80 and W30Ti70 samples. These values are all equal to or slightly below the ones expected from chemical compositions (0.11, 0.25 and 0.43 for, respectively, W10Ti90, W20Ti80 and W30Ti70). In relative contrast, the composite samples show W/Ti ratios both (modestly) above or below the theoretical ones. More precisely they take values of 0.11, 0.24, and 0.48, for respectively, the 0.1, 0.25 and 0.5WO$_3$/TiO$_2$ samples. Absence of other chemical species (particularly nitrogen) was confirmed by chemical analysis.

The XRD patterns of all samples and reference systems are presented in Figure 2. The tetragonal anatase structure (PDF 21-1272; space group I4$_1$/amd) dominates the pure titania reference XRD pattern while the tungsten oxide reference XRD pattern can be indexed into the monoclinic polymorph (PDF 83-0951; space group P2$_1$/n). The so-called doped samples (xWyTi) only display the anatase diffraction pattern, with differences from the titania reference growing with the tungsten content. The width of the peaks clearly grows with tungsten nominal content of the samples. This has been previously observed (43,44,45) and it is a first clear indication of the tungsten cations

located at lattice positions of the anatase structure. Meanwhile absence of tungsten oxide alone contributions is noticed in doped samples, so we did not detect it for a W content equal to or below 30 at. % (cationic basis). This fact is in agreement with the relative large solubility limit of tungsten cations at the anatase structure, typically reported to be in the 20-30 at. % (cation basis) interval (7,8,19,46,47).On the contrary, in the so-called surface sensitized samples, the anatase phase hardly shows any modification and the series displays the presence of monoclinic tungsten oxide for the 0.25 and $0.5WO_3/TiO_2$ samples. The mentioned differences in XRD observables between the anatase phase in doped and composite samples are clearly reflected in the anatase primary particle size values presented in Table 1. They decrease or are essentially constant with tungsten content for, respectively, doped and composite samples. For the composite samples, the monoclinic tungsten oxide does not show variation of the primary particle size with tungsten content when detected by diffraction. The behavior of morphology observables is also included in Table 1. BET area variation through the series of samples correlates with primary particle size of the anatase component; it decreases when size increases and is roughly constant when size does not vary. On the other hand, pore volume and size appear roughly constant in the doped or composite series and decrease from pure titania indicating partial occlusion of the pore system by tungsten species and/or modification by its presence in the catalyst formulation.

Figure 3 shows the aberration corrected HAADF-STEM images of samples 10W90Ti and 20W80Ti as representative examples of doped materials and $0.1WO_3/TiO_2$ and $0.25WO_3/TiO_2$ samples as composite materials. In this type of images, in which the intensity is directly proportional to the square of the atomic number, the presence of W (Z = 74) can easily be differentiated on the titanium (Z = 22) phases. No large aggregates of tungsten oxide are seen in any of the samples, neither in the images displayed in Figure 3 nor in the XEDS maps shown in Figure 4. The combination of results confirms that in all cases the tungsten-containing entities in contact with anatase are highly dispersed on or into the support. In fact, the bright white spots corresponding to tungsten atoms can be clearly seen in the images. These atoms seem to be aligned in some areas with the anatase planes, with almost atomically dispersed units in the case of doped samples and forming small clusters of approximately half a nanometer in the case of the $0.1WO_3/TiO_2$ and $0.25WO_3/TiO_2$ samples. A more detailed description of the tungsten-containing entities is presented below. The XEDS analysis of the samples

shows, on the other hand, the high chemical homogeneity of the samples. Figure 5 displays XEDS analyses (quantitative results) for different regions of the catalysts included in Figure 4. Figure 5 provides evidence of the rather limited variation of chemical composition in the samples at nanometric level. For the four samples presented in Figure 4, the average chemical composition extracted from XEDS (included in Figure 5) may display different from values obtained by chemical analysis. Concretely, differences are encountered in composite catalysts. This comes out from the fact that a fraction of tungsten forms monoclinic WO_3 particles without appreciable contact with the dominant anatase phase. According to XRD, this WO_3 phase appears for a tungsten content corresponding to the $0.25WO_3/TiO_2$ sample. Comparing W/Ti atomic ratios obtained by chemical analysis and XEDS we can estimate that ca. null, 16 and 23 % of tungsten atoms are forming the monoclinic WO_3 aggregates for, respectively, the $0.1WO_3/TiO_2$, $0.25WO_3/TiO_2$ and $0.5WO_3/TiO_2$ samples

As mentioned the details of the surface (and bulk) species of tungsten are crucial as they define the nature (doped vs. composite) of the samples and the physico-chemical properties of the materials. We carefully analyzed the surface composition of the samples by combining X-ray photoelectron and Raman spectroscopies with a microscopy analysis of the surface. Figure 6 shows XPS spectra for the W 4d region while Table 2 summarizes all relevant observables coming from the XPS study. Results in Table 2 showed the exclusive presence of W(VI) and Ti(IV) species with characteristic binding energies of 247.2 (W $4d_{5/2}$) and ca. 458.4 (Ti $2p_{3/2}$) eV (48). The W/Ti atomic ratio provides interesting clues concerning the dispersion state of the tungsten-containing species. For doped samples they are essentially equal to the chemical analysis results. For composite samples we obtain higher values using XPS due to the inherent surface nature of the corresponding tungsten-containing entities as well as the presence of a minor monoclinic WO_3 phase for $0.25WO_3/TiO_2$ and $0.5WO_3/TiO_2$ samples. On the other hand, Raman indicates the exclusive presence of anatase as crystalline phase (result not shown) but we here concentrate in the tungsten species detected (Figure 7). The spectra show peaks at ca. 800-840 and 980 cm^{-1}. The first type of contribution corresponds to W-O-W species, present in monoclinic WO_3 (935 cm^{-1}) as well as surface species presenting W-W bonds (27, 49). In the case of doped samples (Figure 7A), in the low wavenumber region appears a very weak band at around 805 cm^{-1}, superimposed over a small bump characteristic of the titania reference. In the case of composite samples (Figure 7B) the region seems to present two bands

with the second associated with the presence of W. The high wavenumber contribution above mentioned (980 cm^{-1}) is exclusive of the surface zone and correspond to a W=O stretching (49,50,51). The frequency of 980 cm^{-1} is characteristic of octahedral local symmetry and is described at the literature as the tungsten surface species optimizing the promotion effect of titania-based (W-Ti) composite photo-catalysts (25,52). The combination of information coming from the position and intensity of the W-related Raman bands would indicate the aggregation state in the case of nanosized tungsten containing species. The doped samples do not show appreciable W-O-W species and a nearly equal quantity of surface W=O species with tungsten content. This suggests strongly similar tungsten-content surfaces. The composite samples show weak but discernible W-O-W species and an intensity of the W=O contribution growing with the tungsten content (something expected for supported samples) and which is higher than the one corresponding to doped samples with similar W/Ti atomic ratio.

The XPS-Raman spectroscopic analysis of tungsten surface species is in keeping with the fact that doped samples do not show any effect related to the formation of W-O-W link and W/Ti surface (XPS) ratios near the ones corresponding to chemical composition, thus presenting always highly dispersed tungsten at surface positions. This does not occur with the composite samples as even in absence of the pure monoclinic WO_3 phase ($0.1WO_3/TiO_2$ sample) we observe a (weak) W-O-W Raman contribution. To provide a quantitative analysis of the tungsten-containing surface entities and thus to help with the visualization of the ultradisperse surface tungsten species, Figure 8 shows some representative aberration corrected HAADF-STEM images of samples $0.1WO_3/TiO_2$, $0.25WO_3/TiO_2$, W10Ti90, and W20Ti80 after denoising and background subtraction following the procedure described in reference 53 . Micrographs corresponding to composite samples present normalized intensities which can be correlated to the presence of a considerable amount of small aggregates (Figure 8; panels a and b). In the case of doped samples, the displayed intensities suggest the presence of mainly ultradisperse, atomic-like, tungsten species (Figure 8; panels c and d). To confirm this finding a histogram has been generated by segmenting the images using a K means clustering algorithm which determines the cluster size distribution versus the number of segmented elements (results presented in Figure S1). Note how the histograms of composite samples (Figure 8; panels e and f) clearly display a broad cluster size distribution, ranging from 0.2 (which could correspond to isolated W atoms) to above 1.2 nm. On the other hand, the histograms obtained from doped samples

(Figure 8; panels g and h) show a narrower distribution centered at 0.2 nm due to the lower amount of W aggregates. To get a better insight into the distribution of atomic-like species, pair correlation analysis was performed in order to detect neighbors and next nearest neighbors of each isolated atom on the Z-contrast images of sample W20Ti80. This gives a pair correlation function g(r) (Figure 9) which informs about the probability of finding the center of a tungsten atom at a given distance from the center of another (tungsten) atom. This analysis provides an average W-W first distance of 0.275 nm (as well as higher order distances; lower intensity peaks in the pair correlation function) which could correspond to a distorted (110) anatase plane. This further indicates that tungsten atoms appeared at the surface termination of the anatase structure, without significant segregation and formation of W-W links (Figures 8 and 9). In short, we obtained two series of W-Ti samples having a dominant anatase structure and relatively similar morphological properties. Doping samples have surfaces which are characteristic of truly doped samples for W content below 30 at. %. Tungsten appears at specific surface positions of the anatase network (as shown by HAADF-STEM) in these materials with no significant enrichment from the bulk (as shown by XPS). As mentioned, this is a direct consequence of the high solubility limit of tungsten cations at the anatase structure (7,8,19,46,47). Relevant for photo-catalysis, tungsten modifies the anatase band gap (Figure S2, Table 1) through the variation of the conduction band minimum (54,55). For composite samples and according to HAADF-STEM, we obtained well controlled tungsten oxide clusters deposited onto titania surfaces with defined particle size, clearly below 1.2 nm for the analyzed samples. A few tungsten oxide particles with monoclinic-like structure and larger size (Table 1) can be detected but are without contact with anatase. This accounts for up to 23 % of the tungsten in the $0.5WO_3/TiO_2$ sample. For the composite samples, the band gap values presented in Table 1 would be a molar average of the two existing phases anatase and monoclinic WO_3. The low percentage of the latter indicates that the surface contact of tungsten entities and anatase makes a net effect in the conduction and valence band positions and produces observable effects in the "effective" band gap of the anatase-dominated crystalline phase.

3.2. Catalytic performance: quantum efficiency

Figure 10 presents the catalytic behaviour of the doped and composite samples through the measurement of the reaction rate in the photo-transformation of toluene and styrene.

We note that Figure 10 focus the study on the comparative photoactivity of doped and composite samples using the (whole) W/Ti atomic range of existence of the W-Ti binary oxide with anatase structure. Samples above this limit were presented in Figure S3 of the supporting information but are clearly of low significance in the context of this work. The titania reference displays activity for both reactions as previously reported (7-9,15-17). The tungsten oxide reference is not included in the plot. Our titania is among the most active bare anatase systems among the previously tested, with a reaction rate above the one measured for the P25 reference using the same set-up and experimental conditions (8,27). The low activity of the pure monoclinic phase was described previously (7,8,27) and here tested (see Table S1). Together with its limited presence (molar quantity) in (some) composite samples allow dismissing any significant catalytic role of such phase.

As can be observed in Figure 10, doped samples provide higher reaction rates than composite samples for almost all W:Ti compositions. Figure 10 proofs it by plotting the reaction rate vs. the W/Ti chemical composition of the anatase phase (estimated by XEDS). Using the W/Ti atomic ratio from chemical analysis would take into account the WO_3 phase which is essentially inactive. On the contrary using the fraction of tungsten in direct contact with the anatase would allow direct comparison with catalysts synthesized using other methodologies and would thus provide generality to the analysis here presented. So, considering the fraction of tungsten in contact or being part of anatase and thus that can play an active role in promoting the corresponding photo-catalytic reaction, it is clear that doped samples present larger activity and maximize catalytic output for both reactions here tested. The maximum of activity observed for the two series of samples has different physical origins. This point has been previously discussed. In brief, in true doped samples it appears that optimum tungsten content produces limited distortion of the anatase structure (limited changes in cell volume and tetragonallity) but modifies the solid conduction band as well as the surface (formation of Lewis acid sites) properties of the solid, producing benefits in charge excitation, handling and pollutant adsorption (8,20,47,50,51). In the case of composite samples, the size of the tungsten surface clusters and their electronic interaction with the anatase component seem critical for charge separation and handling after excitation as well as for modifying surface properties affecting adsorption of pollutants (27,56,57).

In this work we concentrate on analysing the relative performance of "true" doped vs. composite materials. To have an indubitable answer to this question in the previous

section we demonstrate the true doped (or composite) character of our samples and now consider to settle down such comparison using the efficiency parameter rather than the reaction rate. As described in Equations 4 and 5, the calculation of the efficiency parameter requires the calculation of the superficial rate of photon absorption and the selectivity factor. As the superficial rate of photon absorption is usually not presented in literature reports, we also measured the so-called apparent quantum efficiency (equation 6) according to the IUPAC rules (35). The apparent quantum efficiency is relatively easy to be calculated (at least when compared with the efficiency parameter) and thus would facilitate comparison with previous results. As mentioned above, the second factor, the S factor, is required for comparing results concerning total and partial oxidation catalysts. Here, for example, doped samples display selectivity to CO_2 from toluene/styrene in the 80-90 % interval while composite samples only display a relatively low CO_2 selectivity, around 10-25 %, in all cases (full details of the selectivity are presented in Table S2 at the supporting information section). The favoring of partial vs. total oxidation products for composite samples and the contrary for doped samples corresponds to the general trend observed previously in the literature (7-9,18-20,22,23,27,58). The key point for our purposes is, in any case, the analysis of the number of charge carrier involved in the formation of each reaction product. The factor S calculation has been carried out using the procedure described in ref. 41 which takes into account the balance of mass and charge for each product formation reaction. The different number of charge carrier species for the different products (or for the same product from different reactant molecules) becomes evident from Tables 3 and 4 and further stress that a real comparison between systems would need to consider the number of charge carrier species involved in the formation of each product. An additional point to mention and concerning Table 4 is the 1-phenyl-ethanol product. It is not included in the table as no net charge consumption takes place in its formation. This would come from the fact that it can be formed by a direct hydration of styrene (27).

To facilitate the complex analysis concerning the influence of the different physico-chemical (optical and chemical) parameters inside the efficiency parameter (equation 4), we present a 2D (bidimensional) plot in Figure S4 where the above mentioned different contributions are normalized and displayed as a function of the W/Ti ratio measured by EDXS. In parallel Figures 11 and 12 show apparent and "true" quantum efficiency values for, respectively, toluene and styrene photo-oxidation, and obtained at different levels of calculation (with and without considering the S factor). They correspond to 3D

(tridimensional) plots which may emphasize or help in visualizing trends among the different samples and series.

We first discuss the effect of the three factors included in equation 4 for the calculation of the efficiency. As shown in panels A and D of Figure S4 significant differences are observed between the reaction rate and the (true quantum) efficiency parameters. While for doped samples we observed relatively similar behavior for both toluene and styrene photo-transformations, profound differences affecting both the shape (i.e. behavior through the series) and the maximum of the curves can be detected in the case of the composite samples. At first sight one may expect that a significant change in optical properties (Figure S2; Table 1) would be critical for this but panels B and E of Figure S4 show that they have only moderate influence. The main source of differences between the reaction rate and the efficiency comes out from the selectivity factor (panels C and F of Figure S4). The differences in the product selectivity of the photo-transformation(s) control the quantum efficiency behavior through the two series of samples and make that the reaction rate is not a good indicator of the photo-catalytic properties when comparing catalysts differing in optical and chemical properties.

As a second objective, Figures 11 and 12 attempt to help in visualizing trends among samples. Apparent quantum efficiency values are smaller than "true" quantum efficiency values and display less marked differences. The more interesting point comes from the comparison of the (true) quantum efficiency values. For toluene photo-transformation we first note than doped samples (panel A of Figure 11) provide higher efficiency values than composite samples (panel B of Figure 10). Also, the efficiency trend with tungsten content is drastically modified for both series of samples when calculation is carried out at the strictest level with respect to any other calculation (the plot allow comparison with the calculation of the quantum efficiency without considering the selectivity factor –see arrows- as well as all modes of calculation carried out for the apparent quantum efficiency). Contrarily to the reaction rate (Figure 10A), the measurement of the "true" quantum efficiency (Figure 11B) shows that no activity enhancement with respect to the titania reference is achieved using composite samples as catalysts. Finally, Figure 11 (as Figure S3) provides firm evidence that the ("true" quantum efficiency) trend among the two series of samples is strongly influenced by the selectivity factor.

For styrene photo-transformation (Figure 12), we observe relative similar values for doped and composite samples and a net enhancement of the quantum efficiency (with

respect to titania) for both series, displaying quantum efficiency maximum enhancement factors (with respect to the titania reference) of 1.27 and 1.18 for, respectively the W10Ti90 and $0.1WO_3/TiO_2$ samples using. Again, note that the shape and particularly the position (sample) of the maximum value(s) for the corresponding observable(s) differ if analyzed using the reaction rate (Figure 10B) and efficiency parameters (Figures 12A and B).

We thus observed that doped samples provide significantly higher quantum efficiency values than composite samples for toluene photo-transformation while differences are relatively less important in the photo-transformation of styrene. Optimum performance in all reactions tested is obtained with the W10Ti90 catalyst (closely followed by the W20Ti80 sample), which provides a significant enhancement (efficiency multiplied by 1.28 and 3.45 for, respectively, toluene and styrene) with respect to the corresponding titania (our nanostructured anatase but also P25) reference samples.

4.   Conclusions

In this study we synthesized (relatively) similar high surface area anatase-based tungsten doped and composite materials having a W:Ti molar relation up to 0.5. The characterization of the materials showed that all powders have a dominant anatase component as crystalline phase. Doped materials show tungsten at anatase bulk and surface lattice positions below 30 at. % (W/Ti atomic ratio of ca. 0.43). Essentially, tungsten appears as atomically dispersed at the surface of the doped catalysts. The composite materials showed the presence of a monoclinic WO_3 phase for W/Ti ratios equal to or above 0.25. Nevertheless, this phase accounts for a maximum of ca. 23 % of the tungsten atoms and is catalytically irrelevant. In all composite cases, the tungsten entities contacted with the anatase phase display good homogeneity and limited particle size, below 1.5 nm.

These materials showed activity in the photo-transformation of toluene and styrene. According to the reaction rate both doped and composite samples can improve the performance of the bare titania reference system. The calculation of the quantum efficiency in the stringent form shows however a different picture. While doped samples can improve the performance of anatase by maximum factors (sample W10Ti90) of ca. 1.3 and 3.5 for, respectively, toluene and styrene photo-transformation, none of the composite samples can overperform the anatase reference for both reactions. Only in the

case of styrene, composite samples overperform (by a maximum factor of 1.2, sample $0.1\ WO_3/TiO_2$) the titania reference.

The analysis of the optical and chemical factors influencing the quantum efficiency values indicates the critical role of the latter in shaping the behavior of the efficiency parameter trough our two series of samples and also the relative activity versus the pure anatase reference. Thus, the work shows that the requirement of the full calculation of the quantum efficiency is a must to allow the rigorous analysis of the performance of doped and composite samples. Analysis of the reaction rate or apparent quantum efficiency can drive to misleading interpretations in terms of both the specific sample proving maximum activity and the possibility of improving the performance of the titania reference systems.

Acknowledgements

Supporting Information

Data concerning TEM, UV-visible and catalytic behavior of the samples, together with numerical details used for calculation of the quantum efficiency parameter are presented in the supporting information section.

References

1 A. Kubacka, M. Fernández-García, G. Colón, Chem. Rev., 112 (2012) 1555-1614.

2 J. C. Colmenares, R. Luque, Chem. Soc. Rev., 43 (2014) 765-778.

3 L. Jing, W. Zhou, G. Tian, H. Fu, Chem. Soc. Rev. 42 (2013) 9509–49.

4 X. Li, J. Yu, J. Low, Y. Fang, J. Xiao, X. Chen, J. Mater. Chem. A, 3 (2015) 2485-2534.

5 S. Khan, H. Cho, D. Kim, S.S. Han, K.H. lee, S.-H. Cho, T. Song, H. Choi, Appl. Catal. B 206 (2017) 520-530.

6 Y. Yang, H. Zhong, C. Tian, Res. Chem. Inter. 37 (2011) 91-102.

7 A. Fuerte, M.D. Hernández-Alonso, A.J. Maira, A. Martínez-Arias, M. Fernández-García, J.C. Conesa, J. Soria, G. Munuera, J. Catal. 212 (2002) 1-9.

8 A. Kubacka, M. Fernández-García, G. Colón, J. Catal. 254 (2008) 272–284

9 L. Zhang, Y. Li, H. Xie, H. Wuang, Q. Zhang, J. Nanos. Nanotechnol. 15 (2015) 2944-2951.

10 N Delegan, R. Pandiyan, A. Dirany, P. Drogui, M.A. El Khakani, J. Appl. Phys. 123 (2018) no. 205101.

11 D.-G. Huang, S.-J. Liao, J.-M. Liu, Z. Dang, L. Petrick, J. Photochem. Photobiol. A 184 (2006) 282-288.

12 N. Consuelo, F.S. García, Einsschalg, R.J. Candal, M. Jobbágy, J. Phys. Chem. C 112 (2008) 1094-1100.

13 S.A. Leghari, S. Sajjad, F. Chen, J. Zhang, Chem. Eng. J. 166 (2011) 906-915.

14 Y. Xin, Y. Wang, H. Liu, D. Ma, E. Chen, J. Appl. Phys. 114 (2013) n. 084308

15 M. Khan, P. Jian, J. Li, W. Cao, J. Appl. Phys. 115 (2014) n. 153103.

16 J. Zhen, F.-Q. Xiou, M. Zou, T. Thomas, H. Jian, Y. Tian, M. Yang, Solid. St. Sci. 54 (2016) 49-53.

17 O. Avilés-García, J. Espino-Valencia, R. Romero, J.L. Rico-Cerda, M. Arroyo-Albiter, R. Natividad, Fuel 198 (2017) 31-41.

18 A. Kubacka, G. Colón, M. Fernández-García, Appl. Catal. B 95 (2010) 238-244.

19 A. Kubacka, B. Bachiller-Baeza, G. Colón, M. Fernández-García, Appl. Catal. B 93 (2010) 274-281.

20 A.M. Márquez, J.J. Plata, Y. Ortega, G. Colón, A. Kubacka, M. Fernández-García, J. Phys. Chem. C 116 (2012) 18759-18767.

21 A. Cordero-García, G. Turnes Palomino, L. Hinojosa-Reyes, J.L. Guzmán-Mar, L. Maya-Reviño, A. Hernández-Ramírez, Environ. Sci. Poll. Res. 242 (2017) 4613-4624.

22 A. Fuerte, M.D. Hernández-Alonso, A.J. Maira, A. Martínez-Arias, M. Fernández-García, J.C. Conesa, J. Soria, G. Munuera, Chem. Commun. (2001) 2718-2719.

23 L. Zhang, M. Quin, W. Yu, Q. Zhang, H. Xie, Z. Sun, Q. Shao, X. Guo, L. Hao, Y. Zhang, Z. Guo, J. Electrochem. Soc. 164 (2017) 1086-1090.

24 J.H. Pan, W.I. Lee, Chem. Mater. 18 (2006) 847-853.

25 K.K. Akurchi, A. Vital, J.-P. Dellemann, K. Michalow, T. Granle, D. Ferri, A. Baiker, Appl. Catal. B 79 (2008) 53-62.

26 A. Bojinova, N. Kaneva, A. Eliyas, E. Stoyanova-Eliyas, D. Dimitrov, Reac. Kinet. Mechan. Catal. 120 (2017) 31-41.

27 M.J. Muñoz-Batista, R. Rachwalick, B. Bachiller-Baeza, A. Kubacka, M. Fernández-García, J. Catal. 309 (2014) 428–438.

28 V. Keller, P. Benhanrd, F. Garin, J. Catal. 215 (2003) 129-138.

29 Y.T. Kwon, K.Y. Song, I. Lee, G.J. Choi, Y.R. Do, J. Catal. 191 (2000) 192-199.

30 S.Y. Chai, Y.J. Kim, W.I. Lee, J. Electroceram 17 (2006) 909-912.

31 A.K.L. Sajjad, S. Shamaila, B. Tian, F. Chen, J. Zhang, Appl. Catal. B 11 (2009) 397-405.

32 J.M. Hermanm, M.N. Mozzanega, P. Pitchat, J. Photochem. 22 (1983) 333-343.

33 S.M. Verbruggen, J. Photochem. Photobiol. C 24 (2015) 4–82

34 H. Yahiro, T. Miyamoto, N. Watanabe, H. Yamamura, Catal. Today 120 (2007) 158-162.

35 S.E. Braslavsky, A.M. Braun, A.E. Cassano, A.V. Emeline, M.I. Litter, L. Palmisano, V.N. Parmon, N. Serpone, Pure Appl. Chem., 83 (2011) 931-1014.

36 M.J. Muñoz-Batista, A. Kubacka, M. Fernández-García, ACS Catal. 4 (2014) 63-72.

37 G.K. Willianson, W.H. May, Acta Metall. 1, (1953) 22-29.

38 P. Kubelka, J. Op. Soc. Am. 38 (1948) 448-457.

39 M. Fernández-García, A. Martínez-Arias, J.C. Hanson J.A. Rodriguez, Chem. Rev. 104 (2004) 4063-4105.

40 D.A. Shirley, Phys. Rev. B 5 (1972) 4709-4714.

41 M.J. Muñoz-Batista, A. Kubacka, A.B. Hungría, M. Fernández-García, J. Catal. 330 (2015) 154–166.

42 G.E. Imoberdorf, H.A. Irazoqui, A.E. Cassano, O.M. Alfano, Ind. Eng. Chem. Res. 44 (2005) 6075–6085.

43 M. Fernández-García, A. Martínez-Arias, A. Fuerte, J.C. Conesa, J. Phys. Chem. B 109 (2005) 6075-6083.

44 D.-S. Kim, J.-H. Yang, S. Balaji, H.J. Cho, M.-K. Kim, D.-U. Kang, Y. Dejaouet, Y.-O. Khow, Crys. Eng. Comm. 11 (2009) 1621-1629.

45 M.V. Dozzi, S. Marzurchi, M. Longui, M. Coduri, L. Artigli, E. Selli, Appl. Catal. B 186 (2016) 157-165.

46 A.Y. Choi, Y. Tokamuro, S.H. Cho, C.-H. Han, Mater. Sci. Forum 695 (2011) 129-132.

47 S. Liu, E. Guo, L. Lin, J. Mater. Chem. 22 (2012) 5031-5041.

48 C.D. Wagner, Handbook of x-ray photoelectron spectroscopy: a reference book of standard data for use in x-ray photoelectron spectroscopy, Physical Electronics Division, Perkin-Elmer Corp., 1979.

49 F.D. Hardcastle, I.E. Wachs, J. Raman Spectrosc. 26 (1995) 397-408.

50 A. Kubacka, G. Colón, M. Fernández-García, Catal. Today 143 (2009) 286–292.

51 A. M. Márquez, J.J. Plata, Y. Ortega, J. Fdez. Sanz, J. Phys.Chem. C 115 (2011) 16970−16976.

52 S. Yamazoe, Y. Hitomi, T. Shishido, T. Tanaka, J. Phys. Chem.. C 112 (2008) 6869-6879.

53 M. Mon, M.A. Rivero-Crespo, J. Ferrando-Soria, A. Vidal-Moya, M. Boronat, A. Leyva-Pérez, A. Corma, J.C. Hernández-Garrido, M. López-Haro, J.J. Calvino, A. Credi, D. Armentano, E Pardo, Angew. Chem. Int. Ed. 57 (2018) 6186-6191.

54 A. Folli, J.Z. Bloh, D.E. Macphee, J. Electroanal. Chem. 780 (2016) 367-372.

55 M. Khan, W. Cao, N. Chen, Z. Usman, D.F. Khan, A.M. Touriq, M.A. Khaskheli, Current Appl. Phys. 13 (2013) 1376-1382.

56 G. Ramis, G. Busca, C. Cristiani, L. Lietti, P. Forzatti, F. Bregani, Langmuir 8 (1992) 1744-1749.

57 K. Ueyama, T. Hatta, A. Okemoto, K. Taniya, S. Nishiyama, Res. Chem. Inter. 44 (2018) 629-638.

58 M. Masunga, G.S. Tito, R. Meijboom, Appl. Catal. A 552 (2018) 154-167.

Table1. Main physico-chemical observables of the samples.

Catalyst	TiO2 Crystallite size (nm)	WO3 Crystallite size (nm)	BET surface area (m² g⁻¹)	Pore volume (cm³ g⁻¹)	Pore size (nm)	Band Gap (e⁻V)
Ti-450	11.3	-------	111.9	0.192	5.3	3.14
10W90Ti	10.1	-------	122.7	0.132	3.5	2.87
20W80Ti	9.6	-------	105.2	0.096	3.0	2.83
30W70Ti	9.8	-------	86.2	0.096	3.6	2.80
0.1 WO₃/TiO₂	15.0	-------	70.0	0.059	3.2	2.91
0.25 WO₃/TiO₂	14.7	23.8	72.5	0.057	3.0	2.83
0.5 WO₃/TiO₂	15.4	23.1	67.8	0.058	3.3	2.63
WO₃	-------	26.3	9.6	0.027	7.3	2.38

Table 2. XPS binding energies (eV) and atomic ratios of the samples.

Catalyst	Ti 2p1/2	Ti 2p3/2	W 4d3/2	W 4d5/2	W/Ti Atomic ratio
TiO₂	464.1	458.3	-------	-------	--------
0.1 WO₃/TiO₂	464.0	458.2	259.8	247.2	0.14
0.25 WO₃/TiO₂	464.1	458.3	259.8	247.2	0.32
0.5 WO₃/TiO₂	464.3	458.5	259.8	247.2	0.58
10W-90Ti	464.0	458.2	259.8	247.2	0.11
20W-80Ti	464.2	458.4	259.8	247.2	0.23
30W-70Ti	464.0	458.2	259.8	247.2	0.43
WO₃	--------	--------	259.9	247.3	--------

Table3. Balanced equations for toluene transformation into products.

Toluene Balanced Equation	
Benzaldehyde: $C_7H_8 + O_2 + h^+ + e^- \rightarrow C_7H_6O + H_2O$	6
Carbon dioxide: $C_7H_8 + 9O_2 + 9h^+ + 9e^- \rightarrow 7CO_2 + 4H_2O$	7

Table4. Balanced equations for styrene transformation into products.

Styrene Balanced Equation	
Styrene Oxide: $C_8H_8 + \frac{1}{2}O_2 + \frac{1}{2}h^+ + \frac{1}{2}e^- \rightarrow C_8H_8O$	8
Benzaldehyde: $C_8H_8 + 2O_2 + 2h^+ + 2e^- \rightarrow C_7H_6O + H_2O + CO_2$	9
Carbon dioxide: $C_8H_8 + 10O_2 + 10h^+ + 10e^- \rightarrow 8CO_2 + 4H_2O$	10
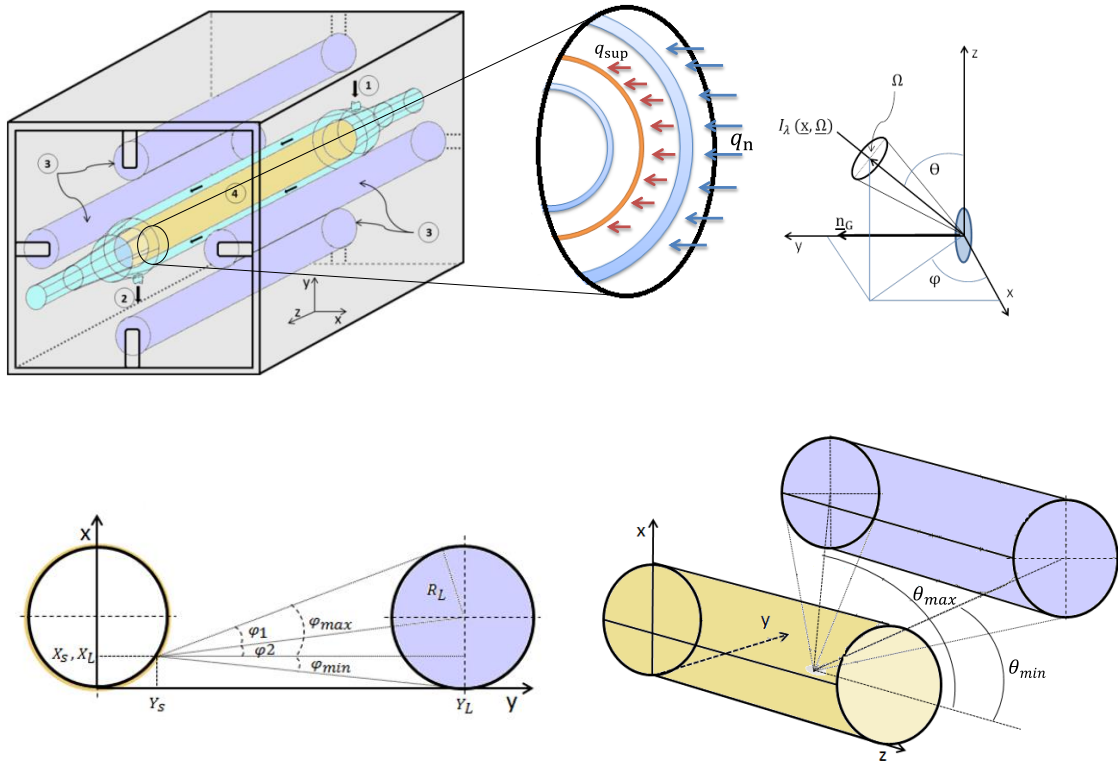
Figure 1. Upper, Left: Photocatalytic annular reactor scheme. (1) gas inlet, (2) gas outlet, (3) lamps, (4) catalyst (brown) sample. q_{sup} radiation flow on the surface of the sample (red), q_n radiation flow from the lamps (blue). Upper, Right: Center of coordinates located at the sample (defined by coordinates x_s, y_s, z_s). Down, Coordinate system to define the integration limits of radiation Model. (Left) φ_{min} and φ_{max}. (Right) θ_{min} and θ_{max}.
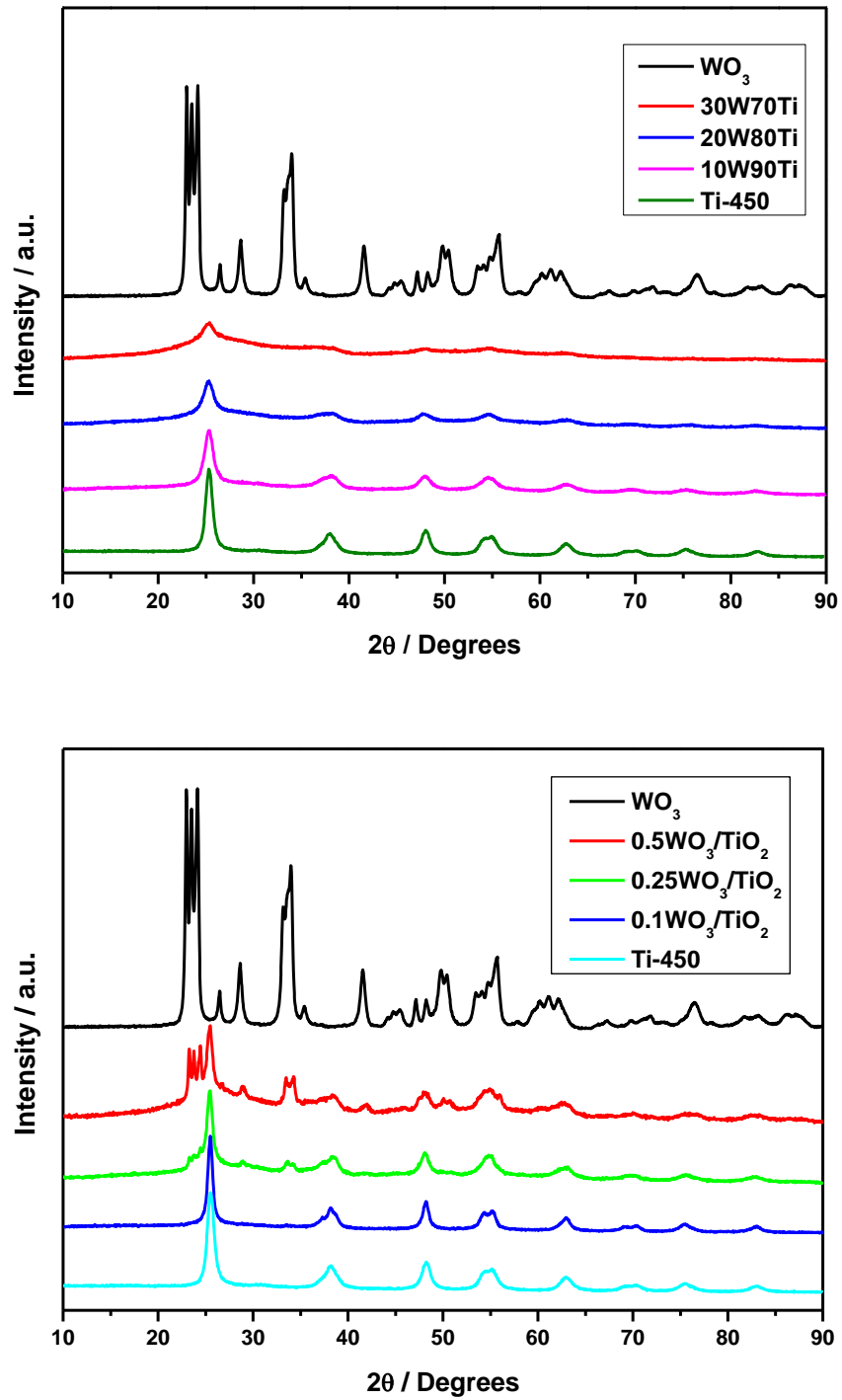
Figure 2. XRD Plots of the samples and references. Upper panel: doped samples; Lower panel; composite samples.
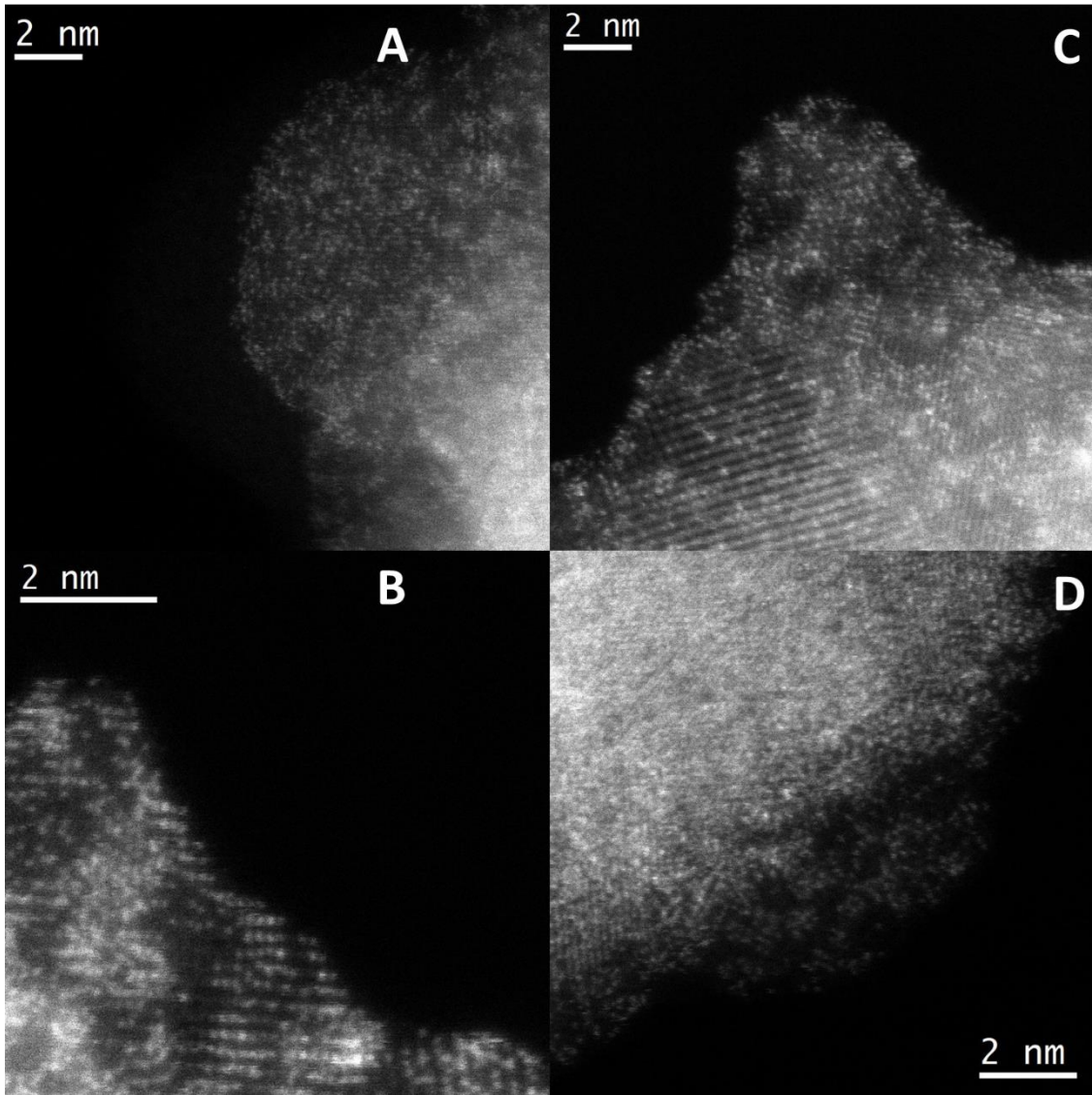
Figure 3. Aberration corrected HAADF-STEM images of A) 10W90Ti, B) 20W80Ti, C) 0.1WO$_3$/TiO$_2$ and 0.25WO$_3$/TiO$_2$
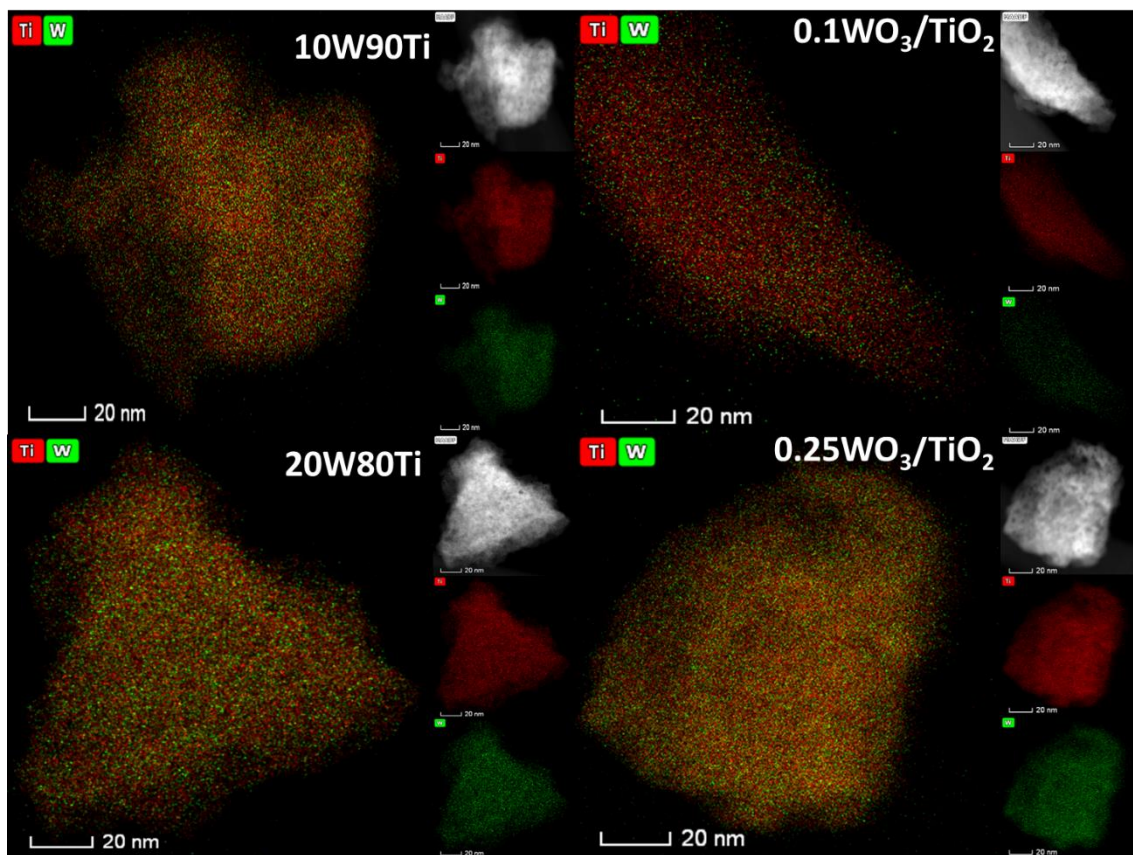
Figure 4. XEDS analysis of selected samples.
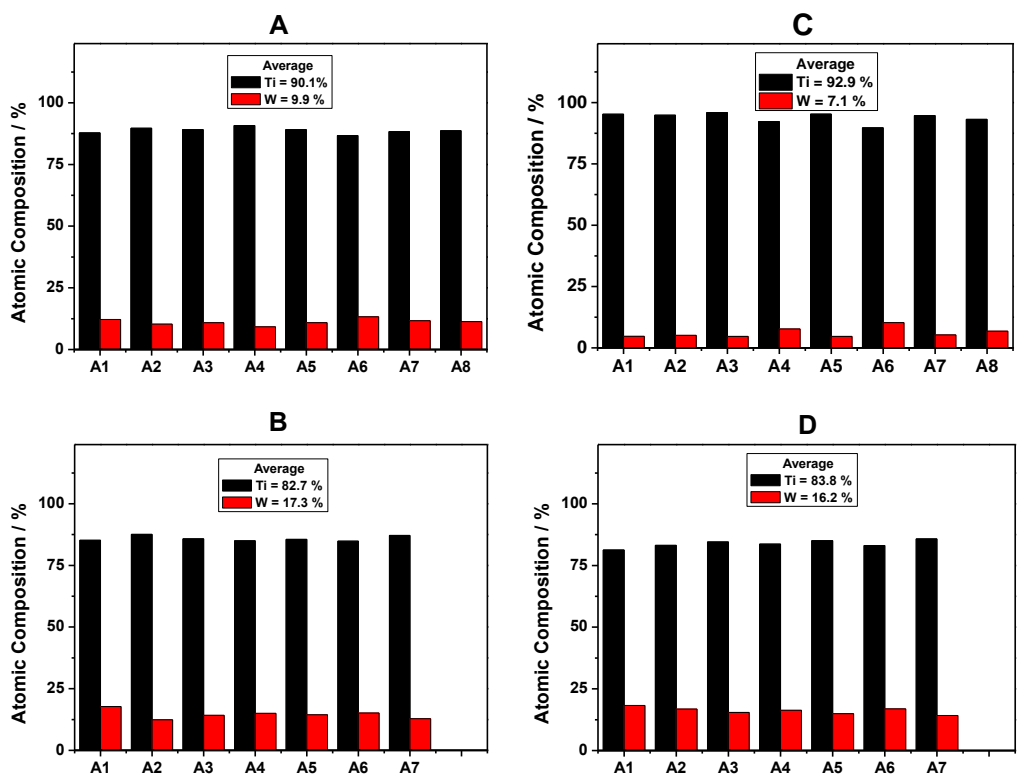
Figure 5. XEDS analyses of ca. 10x10 nm zones of samples: A) 10W90Ti, B) 20W80Ti, C) $0.1WO_3/TiO_2$ and $0.25WO_3/TiO_2$.
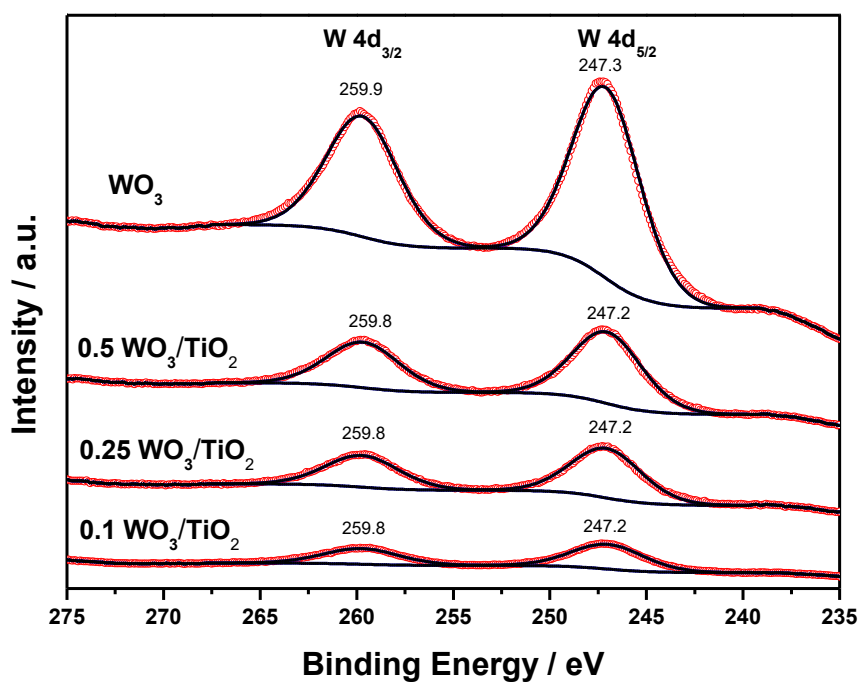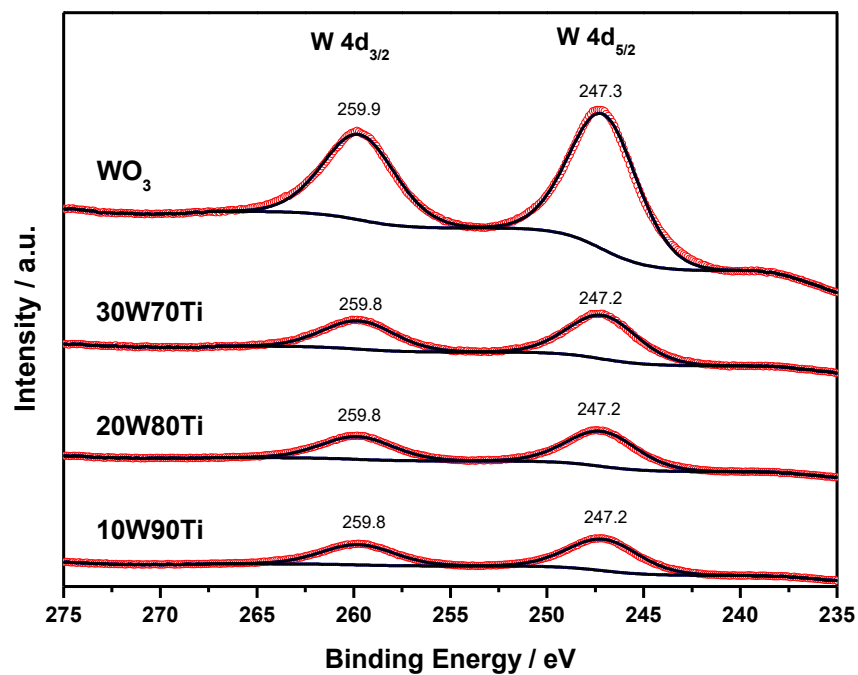
Figure 6. W 4d XPS spectra of the samples and references. Upper panel: doped samples; Lower panel; composite samples.
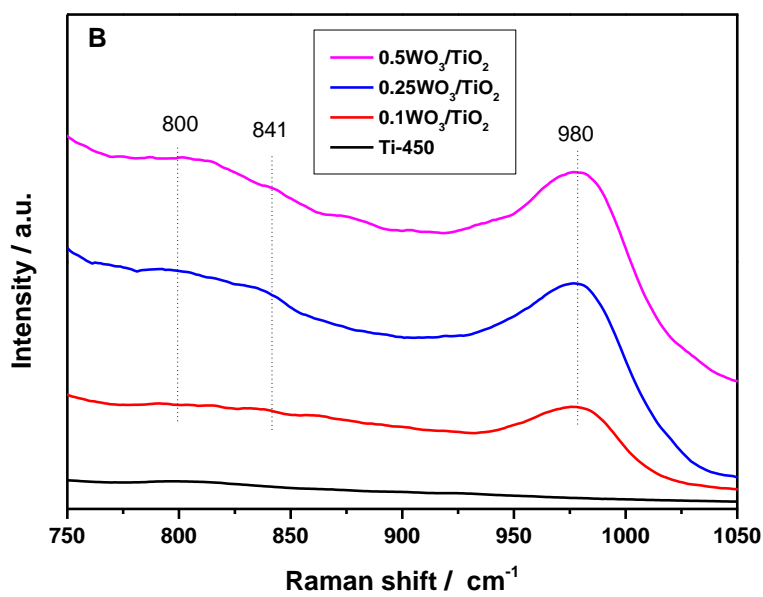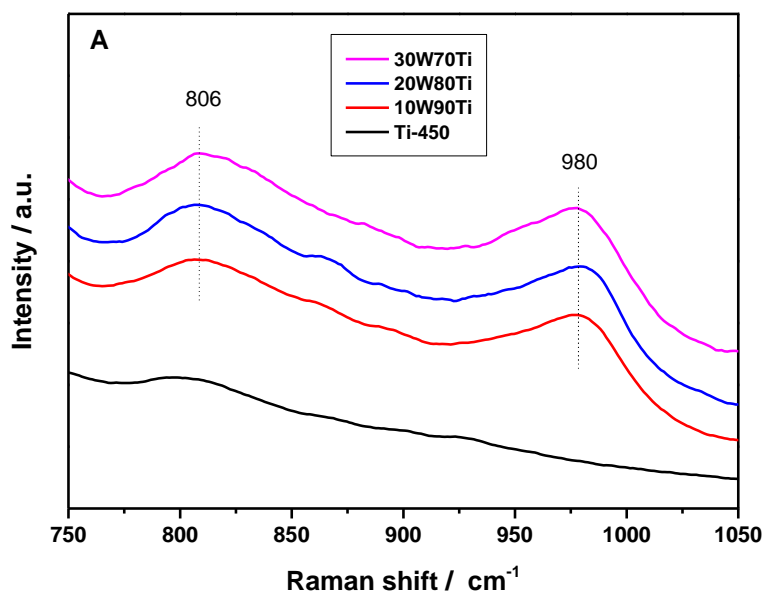
Figure 7. Raman spectra of the samples: (A) doped samples; (B) composite samples. Note the x4 scale factor of A vs. B panel (visible in the titania reference).

A

0.1WO$_3$/TiO$_2$

B

0.25WO$_3$/TiO$_2$

C

W10Ti90

D

W20Ti80

E

F

G

H
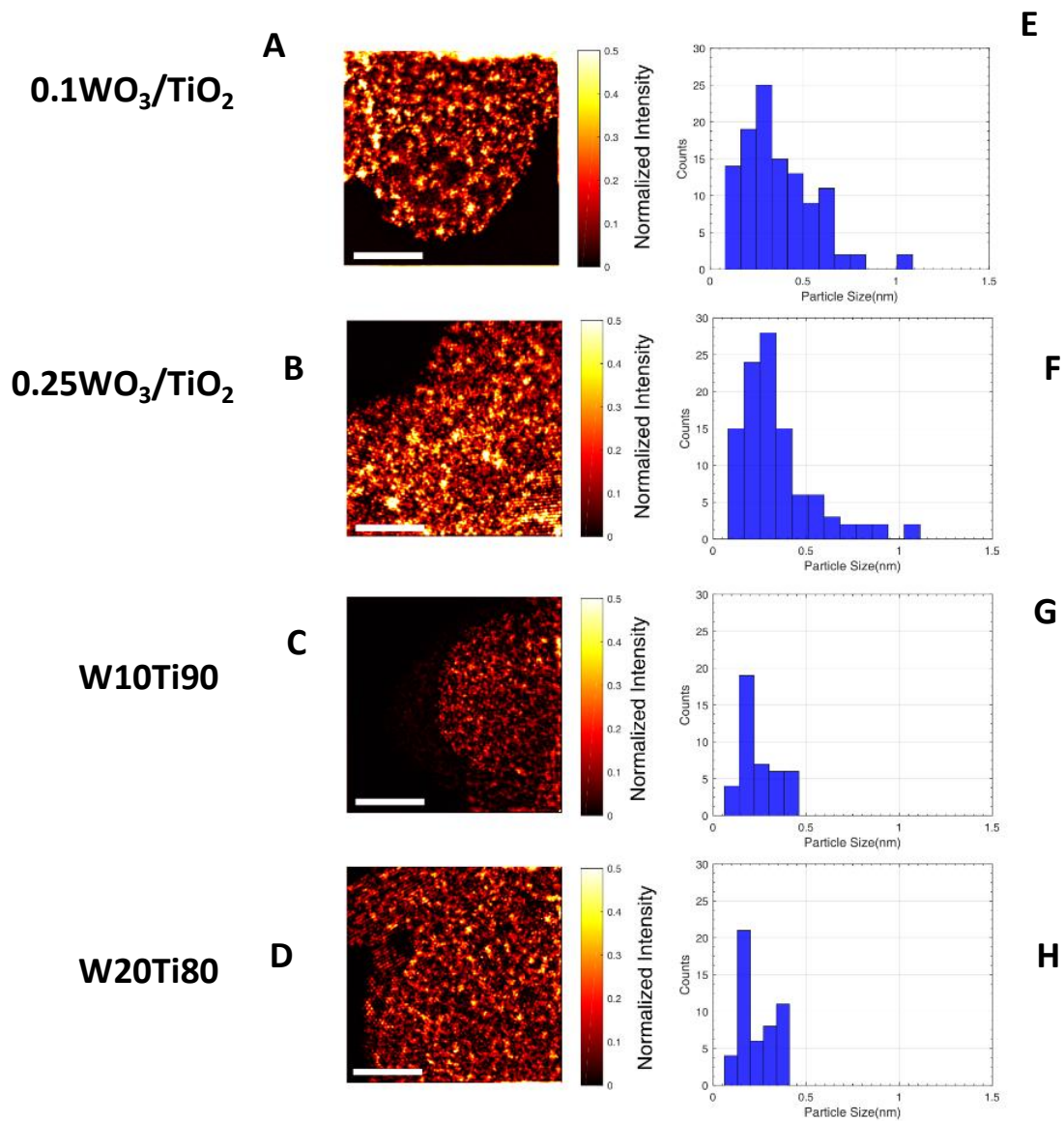
Figure 8. left-hand side: aberration corrected HAADF-STEM images of samples 0.1WO$_3$/TiO$_2$, 0.25 WO$_3$/TiO$_2$, 10W90Ti and 20W80Ti (a,b,c and d, respectively). Scale bar 5nm. Right-side; (e, f, g and h) corresponding particle size distribution.
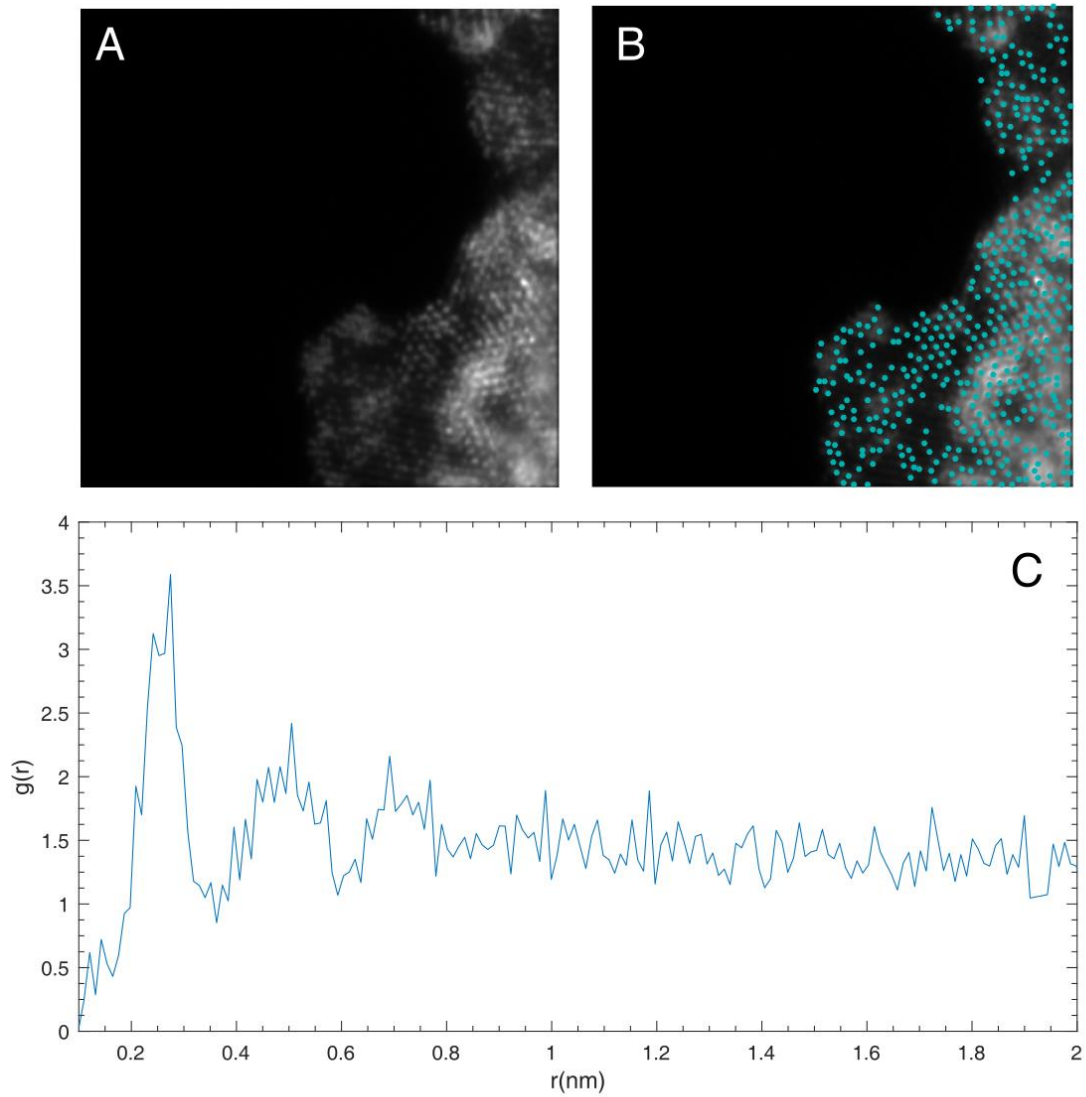
Figure 9. A) De-noised AC-HAADF-STEM image for the 20W80Ti sample. B) Overlay of the de-noised AC-HAADF-STEM image and the xy coordenates (green dots) obtained after template matching. D) The pair correlation function from the processed image.
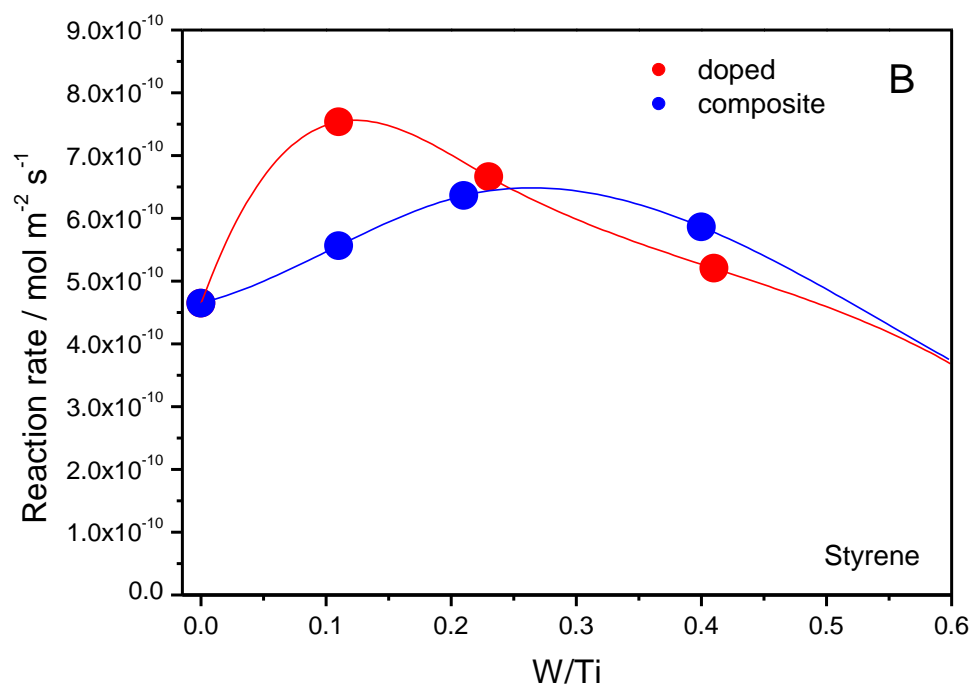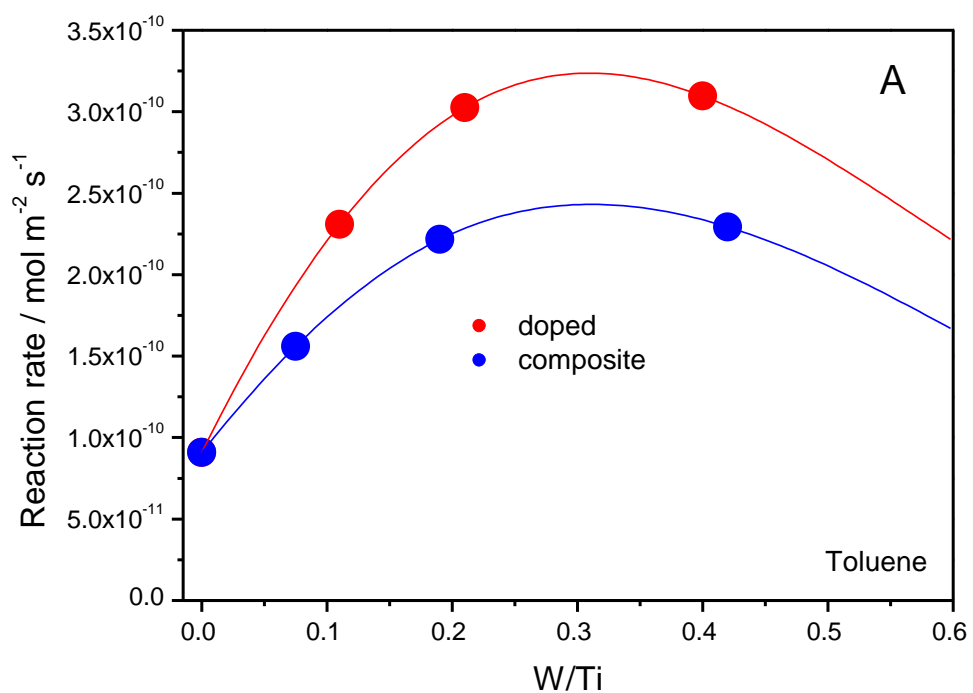
Figure 10. Reaction rate for toluene (A) and styrene (B) photo-transformation. Activity of the samples is presented as a function of the W/Ti atomic ratio measured by XEDS. Lines are only guides for the aids.
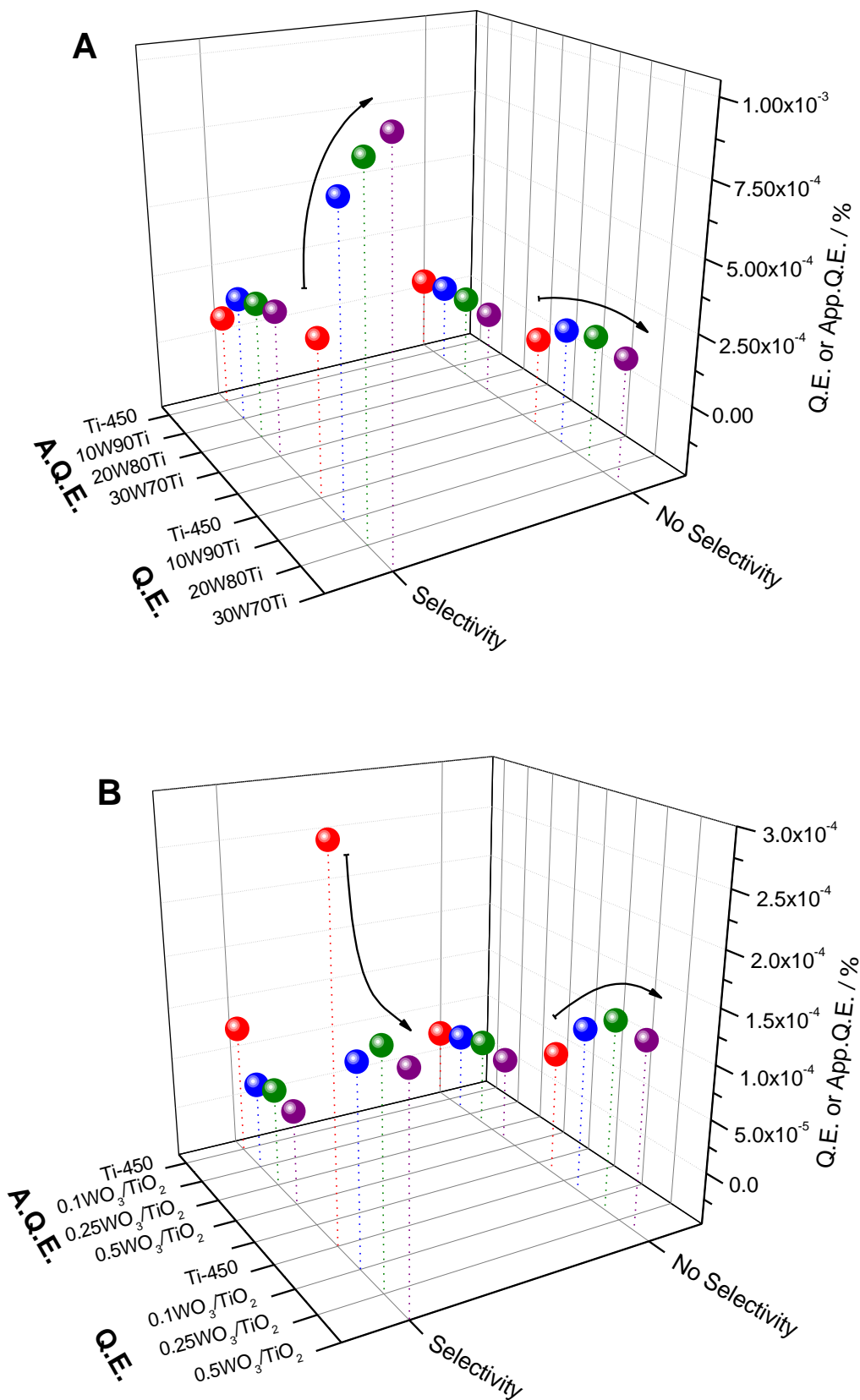
Figure 11. Apparent (A.Q.E.) and True (Q.E.) Quantum Efficiency obtained with/without considering the Selectivity factor for toluene photo-transformation: A) doped materials and B) composite materials.
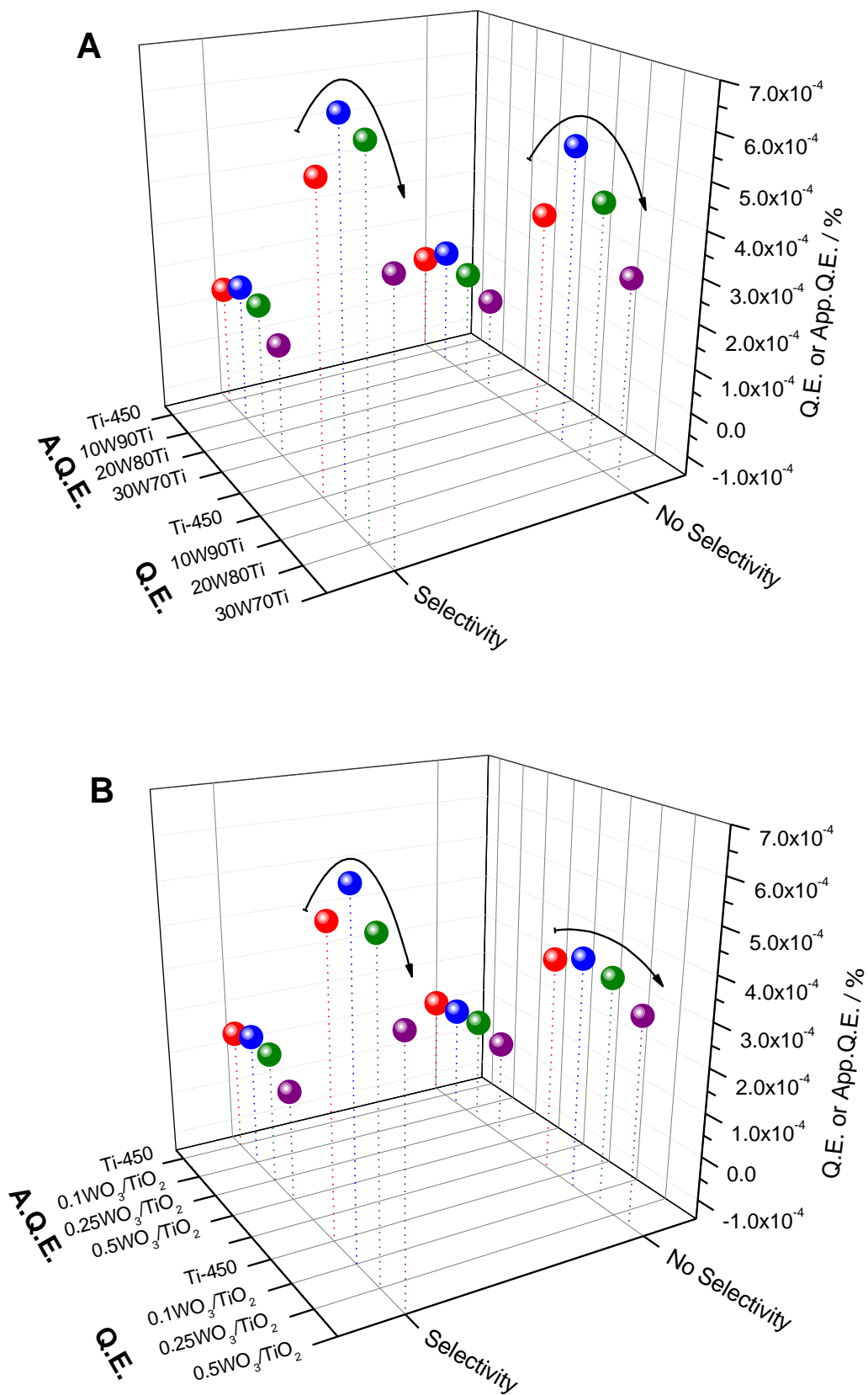
Figure 12. Apparent (A.Q.E.) and True (Q.E.) Quantum with/without considering the Selectivity factor for styrene photo-transformation: A) doped materials and B) composite materials.

Toluene and Styrene Photo-Oxidation Quantum Efficiency: Comparison between Doped and Composite Tungsten-containing Anatase-based Catalysts

Uriel Caudillo-Flores,[1] Mario J. Muñoz-Batista,[1,2] Ana B. Hungría,[3] Miguel López Haro,[3] Marcos Fernández-García,[1,*] Anna Kubacka,[1,*]

1 Instituto de Catálisis y Petroleoquímica, CSIC, C/Marie Curie 2, 28049-Madrid, Spain

2. Departamento de Quımica Organica, Universidad de Cordoba, Edificio Marie-Curie (C-3), Ctra Nnal IV-A, Km 396, Cordoba, Spain.

3. Departamento de Ciencia de Materiales, Ingeniería Metalúrgica y Química Inorgánica, Facultad de Ciencias, Universidad de Cádiz, 11510 Puerto Real, Cádiz, Spain

1.- Detail of integration limits: equation 2

Integration limits of equation 2 are summarized in equations S1-S7 and can be graphically visualized in Figure 1.

$$\varphi_1 = \tan^{-1}\left(\frac{X_L - X_S}{Y_L - Y_S}\right) \tag{S1}$$

$$\varphi_2 = \sin^{-1}\left(\frac{R_L}{(X_L - X_S)^2 + (Y_L - Y_S)^2}\right) \tag{S2}$$

$$\varphi_{min} = \varphi_1 - \varphi_2 \tag{S3}$$

$$\varphi_{max} = \varphi_1 + \varphi_2 \tag{S4}$$

$$\theta_{min}(\varphi) = \cos^{-1}\frac{-Z_S}{(X_{Lm}(\varphi) - X_S)^2 + (Y_{Lm}(\varphi) - Y_S)^2 + Z_S{}^2} \tag{S5}$$

$$\theta_{max}(\varphi) = \cos^{-1}\frac{Z_L - Z_S}{(X_{Lm}(\varphi) - X_S)^2 + (Y_{Lm}(\varphi) - Y_S)^2 + Z_S{}^2} \tag{S6}$$

Where:

$$X_{Lm}(\varphi) = X_L + (X_s - Y_L)\cos\varphi^2 + (Y_L - Y_s)(\cos\varphi\,\sin\varphi) -$$

$$\sin\varphi\sqrt{(R_L{}^2 - (X_s - X_L)\cos\varphi + (Y_L - Y_s)\,\sin\varphi)^2)} \tag{S7}$$

$$Y_{Lm}(\varphi) = Y_{s_i} + (Y_L - Y_s)\cos\varphi^2 + (X_s - X_L)(\cos\varphi\,\sin\varphi) -$$

$$\cos\varphi\sqrt{(R_L{}^2 - (X_s - X_L)\cos\varphi + (Y_L - Y_s)\,\sin\varphi)^2)} \tag{S8}$$

Where symbols were previously defined (main text) except X_L, Y_L, Z_L which are the coordinates of the points located on the surface of the lamp.
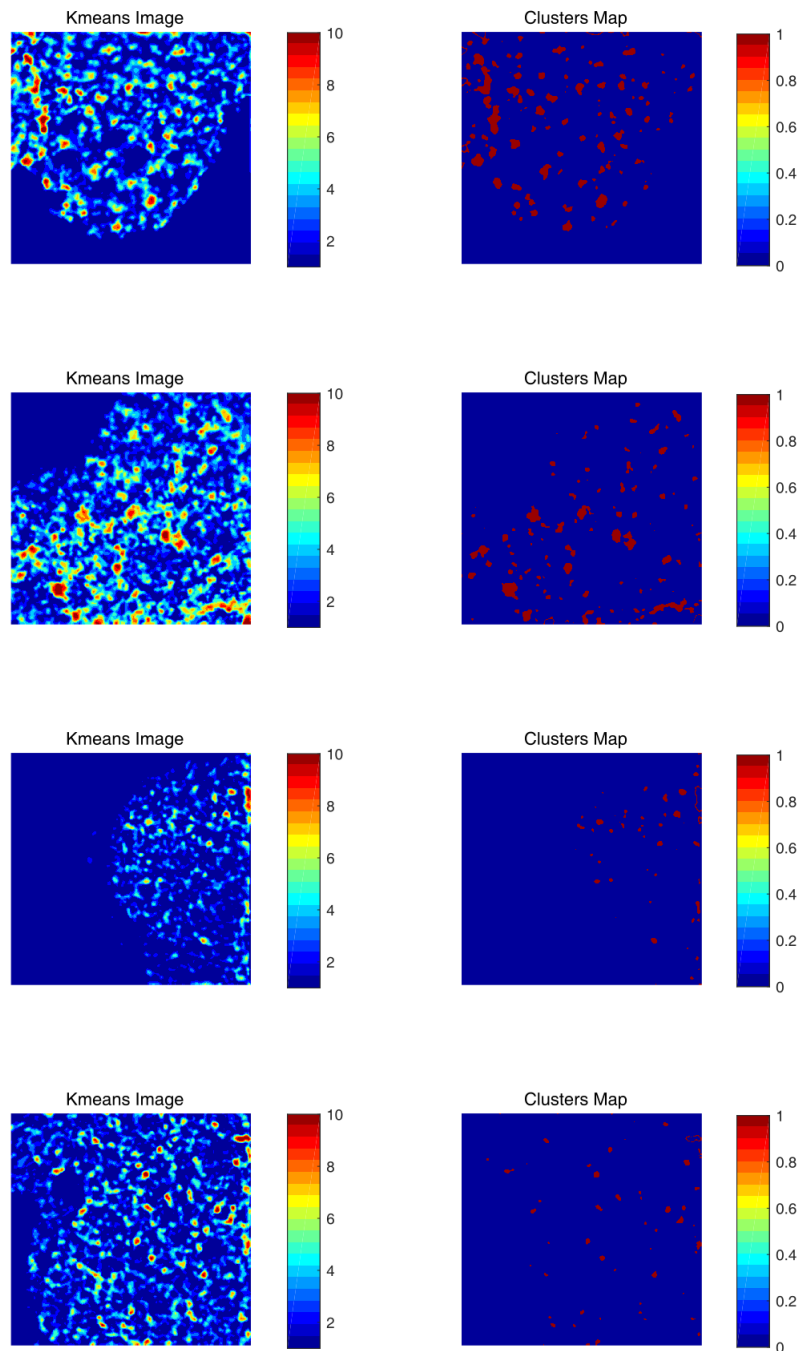
2.- Characterization results

Figure S1. Left-hand side (from top to down): Kmeans segmented images of samples 0.1WO$_3$/TiO$_2$, 0.25 WO$_3$/TiO$_2$, 10W90Ti and 20W80Ti. Scale bar 5nm. Right-side; corresponding clusters maps obtained by thresholding the corresponding Kmeans segmented images.
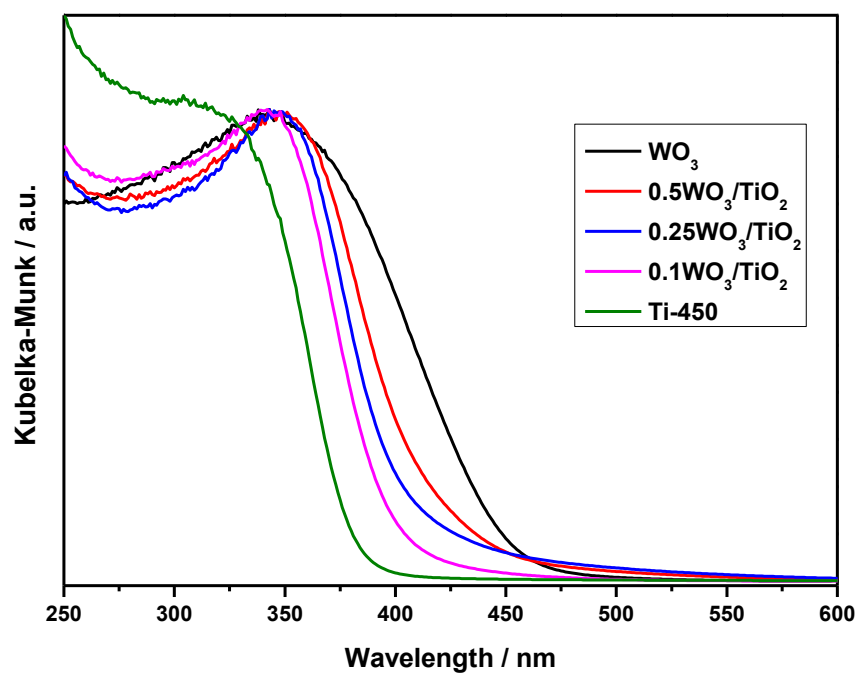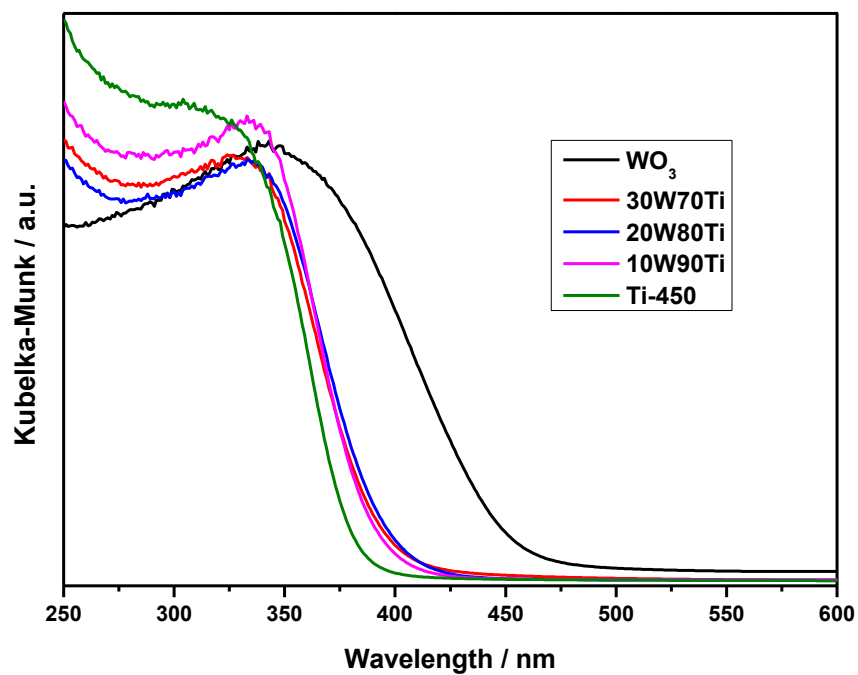
Figure S2. UV-visible spectra of the samples and reference systems.

3.- Catalytic results

Table S1. Reaction rates obtained for references samples.

Test/Sample	Anatase TiO_2 reference	Monoclinic WO_3 reference
	Reaction rate / mol m^{-2} s^{-1}	
Toluene	9.1×10^{-11}	0.8×10^{-11}
Styrene	4.65×10^{-10}	2.2×10^{-11}

Table S2. Selectivity (%) to the different products obtained in the toluene and styrene photo-transformations. Bz: Benzaldehyde; SO; Styrene Oxide; 1PE; 1-phenyl-ethanol.

Samples	Toluene		Styrene			
	Bz	CO_2	Bz	SO	1PE	CO_2
Ti	13.6	86.4	9.3	4.7	-	86.0
W10Ti90	10.8	89.2	4.4	13.0	-	82.6
W20Ti80	11.4	88.6	4.2	5.1	-	90.7
W30Ti70	7.5	92.5	6.0	7.3	-	86.6
0.1 WO_3/TiO_2	78.0	22.0	78.9	6.3	3.2	11.6
0.25 WO_3/TiO_2	77.5	22.5	73.2	9.3	3.1	14.4
0.5 WO_3/TiO_2	76.5	23.5	57.3	16.4	6.6	19.7

Note that according to equations 8 to 10 (main test) carbon dioxide generation takes place using several reaction paths in the case of styrene. This needs to be considered in the calculation of the selectivity factor.
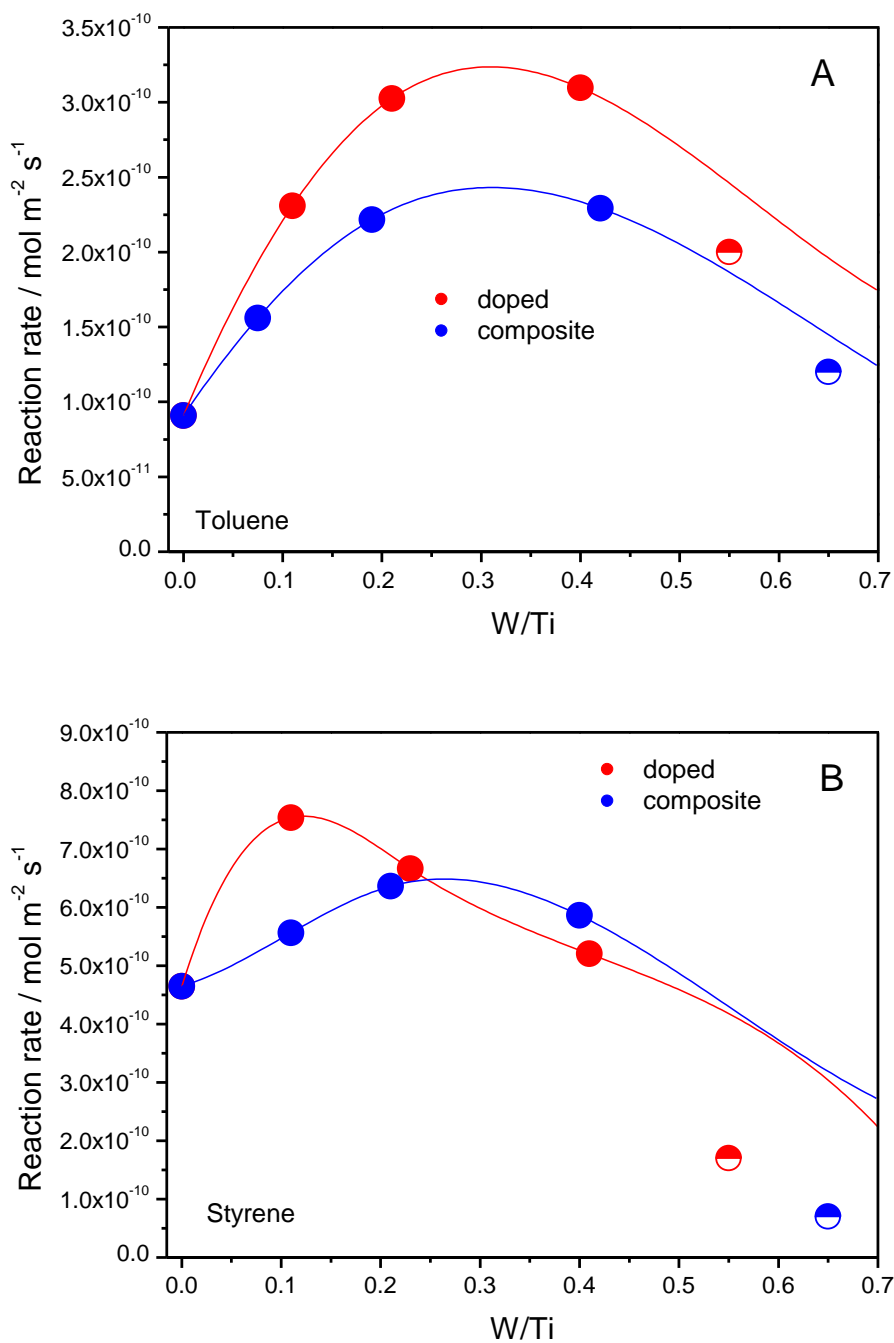
Figure S3. Reaction rate for toluene (A) and styrene (B) photo-transformation. Activity of the samples is presented as a function of the W/Ti atomic ratio measured by XEDS. Lines are only guides for the aids.

Not that Figure S3 is the same of Figure 10 (main paper) but including secondary samples (samples W40Ti60 and 1.0 WO_3/TiO_2, catalytic output presented using semi-filed symbols). In particular and concerning doped samples, Figure S3 includes a sample having tungsten species at bulk and surface positions of anatase as well as tungsten oxide aggregates without contact with the anatase phase.
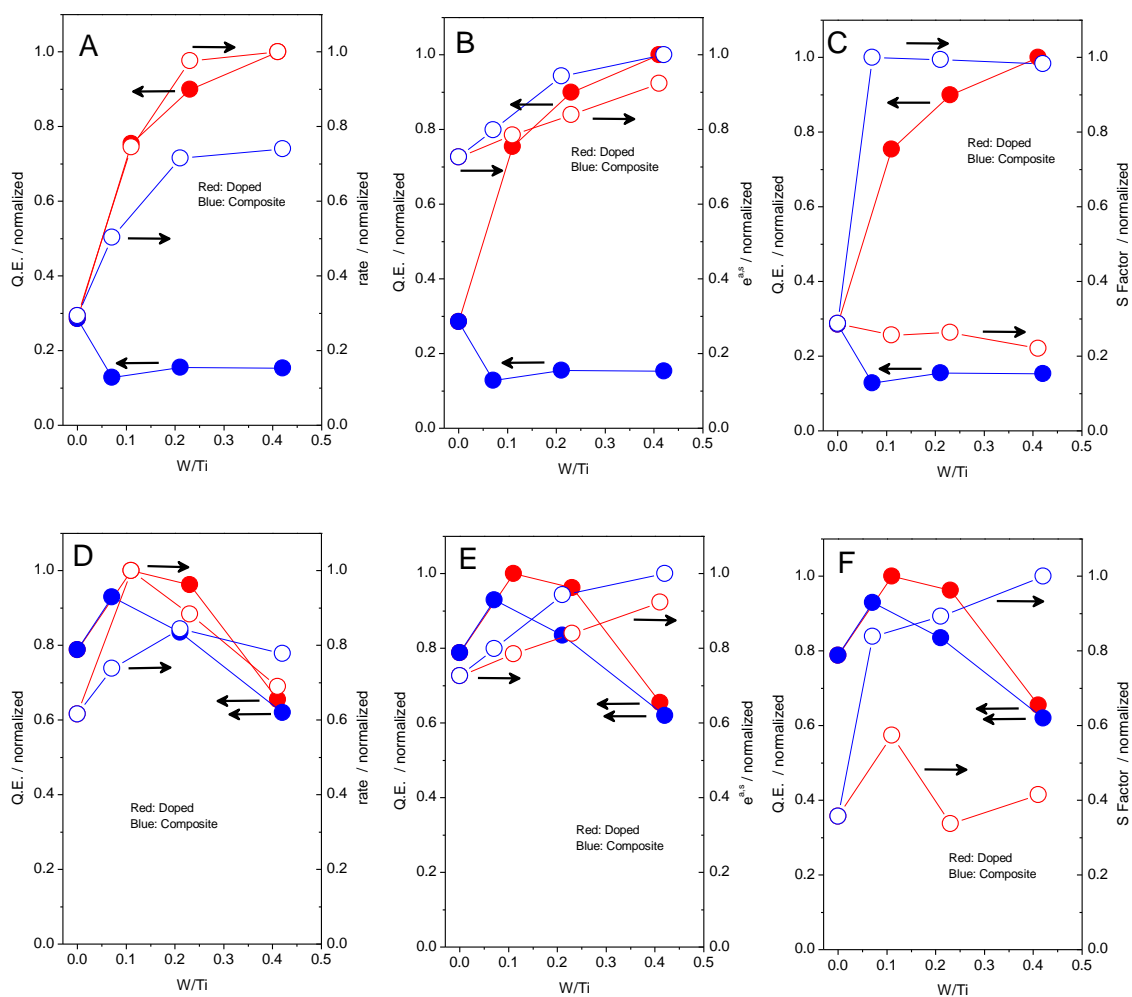
Figure S4. Plot showing the evolution of (normalized) reaction rate, local rate of photon absorption, selectivity factor (right OY axis) and quantum efficiency (left OY axis) observables vs. the W/Ti atomic ratio measured by XEDS. Upper row: Toluene photo-degradation (A, B, C); Lower row: Styrene photo-degradation (D, E, F).

Normalization is carried out by giving unity value to the maximum values of each observable in the panels. This facilitates comparison.